JGR Solid Earth

RESEARCH ARTICLE
10.1029/2021JB023281

An Efficient and Stable High-Resolution Seismic Imaging Method: Point-Spread Function Deconvolution

Jidong Yang[1], Jianping Huang[1], Hejun Zhu[2], George McMechan[2], and Zhenchun Li[1]

[1]Department of Geophysics, China University of Petroleum, Qingdao, China, [2]Department of Geosciences, The University of Texas at Dallas, Dallas, TX, USA

Key Points:

- Conventional least-squares migration is too expensive to be widely applied for large-scale problems under current computational capacity
- An efficient approach for calculating point-spread functions using local modeling and migration is proposed
- The point-spread function deconvolution is then applied to incorporate the Hessian effect and improve image quality

Correspondence to:
J. Yang and J. Huang,
jidong.yang@upc.edu.cn;
jphuang@upc.edu.cn

Citation:
Yang, J., Huang, J., Zhu, H., McMechan, G., & Li, Z. (2022). An efficient and stable high-resolution seismic imaging method: Point-spread function deconvolution. *Journal of Geophysical Research: Solid Earth*, *127*, e2021JB023281. https://doi.org/10.1029/2021JB023281

Received 19 SEP 2021
Accepted 24 JUN 2022

Author Contributions:
Conceptualization: Jidong Yang
Investigation: Jidong Yang, Hejun Zhu, George McMechan
Methodology: Jidong Yang, Hejun Zhu, George McMechan
Software: Jidong Yang
Supervision: Jianping Huang, Hejun Zhu, Zhenchun Li
Validation: Jidong Yang
Visualization: Zhenchun Li
Writing – original draft: Jidong Yang
Writing – review & editing: Jidong Yang, Jianping Huang, Hejun Zhu, George McMechan

Abstract By fitting observed data with predicted seismograms, least-squares migration (LSM) computes a generalized inverse for a subsurface reflectivity model, which can improve image resolution and reduce artifacts caused by incomplete acquisition. However, the large computational cost of LSM required for simulations and migrations limits its wide applications for large-scale imaging problems. Using point-spread function (PSF) deconvolution, we present an efficient and stable high-resolution imaging method. The PSFs are first computed on a coarse grid using local ray-based Gaussian beam Born modeling and migration. Then, we interpolate the PSFs onto a fine-image grid and apply a high-dimensional Gaussian function to attenuate artifacts far away from the PSF centers. With 2D/3D partition of unity, we decompose the traditional adjoint migration results into local images with the same window size as the PSFs. Then, these local images are deconvolved by the PSFs in the wavenumber domain to reduce the effects of the band-limited source function and compensate for irregular subsurface illumination. The final assembled image is obtained by applying the inverse of the partitions for the deconvolved local images. Numerical examples for both synthetic and field data demonstrate that the proposed PSF deconvolution can significantly improve image resolution and amplitudes for deep structures, while not being sensitive to velocity errors as the data-domain LSM.

Plain Language Summary Seismic imaging is an important tool to detect hydrocarbon resource and study deep Earth's structure. Traditional ray-based and wave equation imaging methods commonly extrapolate observed data and apply appropriate imaging condition to construct subsurface impedance interfaces. Mathematically, these methods can be considered as adjoint operators of seismic modeling, but they have difficulty to produce high-quality images of complicated subsurface structures. To mitigate this issue, we present an efficient and stable high-resolution imaging approach, i.e., the point-spread function (PSF) deconvolution. The locally temporal and spatial limitations are utilized to efficiently compute the PSFs on a coarse grid using a ray-based Gaussian beam propagator. Then, an on-the-fly interpolation on a fine grid and a wavenumber-domain deconvolution are applied to improve image resolution. Numerical experiments for benchmark model and field data demonstrate the feasibility and adaptability of the proposed method for imaging complicated salt structure and low-signal-to-noise data.

1. Introduction

Seismic imaging plays an important role in hydrocarbon detection and study of deep Earth's structure (Claerbout, 1985; Freeman et al., 1988; Gray, 2001). It extrapolates observed data in reverse time and applies an appropriate imaging condition to reconstruct subsurface impedance interfaces. In the past 30 years, with the rapid development of computing technologies, seismic imaging methods have evolved from early ray-based Kirchhoff migration (Gray & May, 1994; Hokstad, 2000; Keho & Beydoun, 1988; Wiggins, 1984), through one-way wave equation migration (Gazdag, 1978; Stoffa et al., 1990; Zhang et al., 2005), and then to current reverse-time migration (Baysal et al., 1983; McMechan, 1983; Nguyen & McMechan, 2015; Sun & McMechan, 2001; Yan & Sava, 2008). Although the accuracy of numerical solvers for the wave equation was greatly improved during the evolution of the algorithms, the basic physical frameworks of these imaging methods is conceptually similar, and can be considered mathematically as an adjoint operator of seismic forward modeling. It is difficult for them to produce high-quality images for complicated subsurface structures, because of band-limited sources and receiver wavefields, incomplete data acquisition, and irregular subsurface illumination.

Tarantola (1984a, 1984b) incorporated seismic imaging into a generalized inversion scheme and proposed to estimate seismic model parameters by fitting observed data with simulated seismograms. The nonlinear inversion, i.e.,

full-waveform inversion (Pratt et al., 1998; Virieux & Operto, 2009), aims to construct seismic velocity, density, attenuation, and anisotropy in a broad wavenumber band, while the linearized waveform inversion, which is later known as least-squares migration (LSM), estimates the high-wavenumber model parameters in a least-squares sense. Because direct computation of LSM solution is too expensive, the gradient-based methods, such as steepest descent and conjugate gradient, are usually used to fit observed records with the predicted seismograms (Fomel et al., 2008; Nemeth et al., 1999; Wang et al., 2013; Wong et al., 2015). Currently, the data-domain LSM has been implemented using a variety of different ray-based and wave equation migration methods (Dai et al., 2011, 2012; Xue et al., 2016; Yang & Zhang, 2019; Yang et al., 2018; Zhang & Schuster, 2014), and extended to (an)elastic and anisotropic media (Dutta & Schuster, 2014; Feng & Schuster, 2017; Ren et al., 2017; Yang et al., 2020). These developments make LSM a robust imaging method and so has been gradually applied to field data processing (Latter et al., 2018; Lu et al., 2018; Wong et al., 2011; Zhang et al., 2015), which produces superior imaging results in comparison to traditional adjoint migration. However, many iterations of data-domain LSM require a large number of forward simulations and adjoint migrations to converge to a good solution, which is still expensive and difficult to be widely used for large-scale models in production under current computational capacity.

To alleviate computational cost, many optimization strategies have been proposed to accelerate the convergence of LSM. For instance, a true or approximated diagonal Hessian is commonly used as a preconditioner for the misfit gradient to compensate for limitations in deep illumination (Plessix & Mulder, 2004; Rickett, 2003; Shin et al., 2001). Guitton (2004) computes a bank of nonstationary matching filters to approximate the Hessian inverse, and applies them to 3D LSM to speed up the convergence (Guitton, 2017). Aoki and Schuster (2009) introduce a deblurring filter into LSM and obtain similar results to standard LSM with less than one-third of the cost. Hou and Symes (2015) derive a Born inversion operator in the subsurface offset domain using the asymptotic approximation and design a weighted conjugate gradient algorithm to accelerate the convergence of extended LSM. Recently, Yang et al. (2021) approximate the Gauss-Newton Hessian with a space-wavenumber filter, which allows LSM to converge to a good solution in four or five iterations.

An alternative for data-domain LSM is to solve the least-squares inverse problem in the image domain as $\mathbf{Hm} = \mathbf{I}$, where $\mathbf{H}$ is the Hessian matrix, $\mathbf{m}$ is the expected reflectivity model, and $\mathbf{I}$ is the traditional adjoint migration image. Theoretically, one column of the Hessian can be computed using one pass of Born modeling and adjoint migration over all sources and receivers. In seismic imaging, even 2D models typically have millions of grid points and 3D models have tens of billions of grid points, which make it prohibitively expensive to directly compute the Hessian. Thus, the core of image-domain LSM is how to efficiently calculate the Hessian matrix. By limiting the imaging region near hydrocarbon reservoirs, Valenciano et al. (2006) proposes a target-oriented wave-equation inversion and considerably reduces the size of Hessian matrix. Tang (2009) introduces plane-wave and random phase encoding into the Hessian computation to further reduce the computational cost. Using the Born modeling and reverse-time migration, Fletcher et al. (2016) calculate point-spread functions (PSFs) on a sparsely distributed seed grid to approximate the Hessian. Guo and Wang (2019) approximate the Hessian matrix with nonstationary filters by comparing a reference image with a demigration/remigration image, and develop an image-domain LSM scheme with a sparsity constraint. However, one common issue in the PSF calculation is the trade-off between fine-enough sampling to capture their spatial variations associated with heterogeneities, and the sufficient sparsity to avoid overlapping of PSFs. As analyzed by Fletcher et al. (2016), these two competing requirements cannot always be reconciled, and additional modeling and migration are needed to generate more PSFs.

In this study, we propose an efficient method to calculate PSFs and utilize the PSF deconvolution to improve the image quality for complicated subsurface structures. With the Green's function computed using Gaussian beam summation, we develop a local Born modeling and migration scheme to compute the PSFs on a coarse grid. The spacing of the coarse grid is set as five to eight times of the fine image sampling increment in order to capture fluctuations in illumination and blurring of the image. In addition, the point scattering responses in the Born modeling are saved only in a short time window, and the cross-correlation used to compute the PSFs is performed only in a window with a length about one wavelength. These localized features in modeling and migration enable significantly reduction of computational costs, while avoiding the overlapping, with sufficient PSF sampling. Then, a multidimensional Gaussian function is applied to the PSFs to attenuate artifacts far away from the PSF centers. Using the partition of unity, which is a collection of window functions that sum to one everywhere in the domain of interest, we decompose the traditional adjoint migration results into a series of local images.

Finally, these local images are deconvolved by the PSFs in the wavenumber domain to alleviate the effects of geometric spreading and the band-limited source functions. Numerical examples, using both synthetic and field data, demonstrate that the proposed method can significantly improve image resolution and amplitudes for deep structures, while not being sensitive to velocity errors as data-domain LSM.

2. Method

2.1. Review of Data-Domain and Image-Domain LSM

Full-waveform seismic modeling can be expressed as

$$\mathbf{RF}(\mathbf{m}) = \mathbf{d}, \tag{1}$$

where $\mathbf{F}$ is a full-wavefield modeling operator, $\mathbf{R}$ is a restriction operator associated with receiver distributions, $\mathbf{m}$ contains the model parameters, and $\mathbf{d}$ is the synthetic data. Based on the Born approximation for the model parameters and seismic data as

$$\mathbf{m} \approx \mathbf{m}_0 + \mathbf{m}_1, \quad \mathbf{d} \approx \mathbf{d}_0 + \mathbf{d}_1, \tag{2}$$

Equation 1 can be simplified to a linear operator (Tarantola, 1984b)

$$\mathbf{RL}\left(\mathbf{m}_0\right)\mathbf{m}_1 = \mathbf{d}_1, \tag{3}$$

where $\mathbf{m}_0$ and $\mathbf{m}_1$ denote the background and perturbed models (e.g., P wave velocity v and density ρ), $\mathbf{d}_0$ and $\mathbf{d}_1$ denote the background and first-order scattering data, $\mathbf{L}(\mathbf{m}_0)$ is a linearized modeling operator that only depends on the background model. In LSM, the first-order scattering data $\mathbf{d}_1$ is usually used to approximate primary reflections, and the high-wavenumber perturbation $\mathbf{m}_1$ is generally defined as the reflectivity model. The least-squares solution for $\mathbf{m}_1$ can be calculated by solving a data fitting problem such as

$$J(\mathbf{m}_1) = \frac{1}{2}\|\mathbf{RLm}_1 - \mathbf{d}_{obs}\|^2, \tag{4}$$

where $\mathbf{d}_{obs}$ is the observed data, $\mathbf{m}_1$ is the high-wavenumber velocity perturbation and is usually considered as the reflectivity model, and the background model in $\mathbf{L}(\mathbf{m}_0)$ is ignored in Equation 4. The normal equation of the misfit function $J(\mathbf{m}_1)$ can be derived by setting $\partial J/\partial m_1 = 0$, which yields

$$\mathbf{L}^\dagger\mathbf{R}^\dagger\mathbf{RLm}_1 - \mathbf{L}^\dagger\mathbf{R}^\dagger\mathbf{d}_{obs} = 0, \tag{5}$$

which $\mathbf{L}^\dagger$ is traditional migration operator and can be considered as the adjoint of linearized modeling operator, and $\mathbf{R}^\dagger$ is the adjoint restriction operator and denotes loading data at receiver locations in migration. By defining the Hessian matrix as

$$\mathbf{H} = \mathbf{L}^\dagger\mathbf{R}^\dagger\mathbf{RL}, \tag{6}$$

the data-domain LSM solution can be written as

$$\mathbf{m}_1 = \mathbf{H}^{-1}\left(\mathbf{L}^\dagger\mathbf{R}^\dagger\mathbf{d}_{obs}\right). \tag{7}$$

With $\mathbf{L}$ and $\mathbf{L}^\dagger$ operators, Equations 6 and 7 can be numerically solved using local optimization algorithms, such as steepest-descent and conjugate gradient methods (Allwright, 1976; Meza, 2010; Scales, 1987). Each iteration requires a pair of Born modeling and adjoint migration, and commonly dozens to hundreds of iterations are needed to converge to an accurate solution, which is still too expensive for large-scale problems under current computational condition.

In image-domain LSM, the forward problem can be expressed by reformulating Equation 5 as

$$\mathbf{Hm}_1 = \mathbf{I}, \tag{8}$$

where $\mathbf{I} = \mathbf{L}^\dagger\mathbf{R}^\dagger\mathbf{d}_{obs}$ is the image computed using traditional adjoint migration. The misfit function for the image-domain LSM can be written as

$$\chi(\mathbf{m}_1) = \|\mathbf{H}\mathbf{m}_1 - \mathbf{I}\|^2. \tag{9}$$

The least-squares solution of Equation 9 is

$$\mathbf{m}_1 = \left(\mathbf{H}^\dagger\mathbf{H}\right)^{-1}\mathbf{H}^\dagger\mathbf{I}, \tag{10}$$

where superscript † denote the conjugate transpose. By reordering Equation 10, we obtain $\mathbf{m}_1 = \mathbf{H}^{-1}\mathbf{I}$, which is equivalent to the data-domain LSM solution. Once the Hessian matrix is computed, Equation 10 can be computed using gradient-based methods. One column of the Hessian matrix can be numerically calculated using the Hessian vector product as

$$\mathbf{H}\mathbf{v} = \mathbf{L}^\dagger\mathbf{L}\mathbf{v}, \tag{11}$$

where $\mathbf{v}$ is a point scatterer vector. The right-hand side of Equation 11 reveals that calculating each column of the Hessian requires one modeling and migration sequence. Thus, it is too expensive to directly compute the entire Hessian for a model with a large number of grid nodes, and in image-domain LSM, the key step is to efficiently calculate the Hessian matrix.

2.2. The Hessian Matrix and PSF in an Acoustic Medium

In an acoustic medium, the synthetic data can be calculated as

$$d\left(\mathbf{x}_r;\mathbf{x}_s,t\right) = \int_0^T f\left(t-t'\right)G\left(\mathbf{x}_r;\mathbf{x}_s,t'\right)dt', \tag{12}$$

where $f(t)$ is the source wavelet, $\mathbf{x}_s$ denotes the source location, $\mathbf{x}_r$ denotes the receiver location, and T is the record duration. $G(\mathbf{x}_r;\mathbf{x}_s,t)$ is the Green's function and can be computed by solving the following wave equation:

$$\frac{1}{\rho(\mathbf{x})v^2(\mathbf{x})}\frac{\partial^2 G(\mathbf{x},t)}{\partial t^2} - \nabla\cdot\left(\frac{1}{\rho(\mathbf{x})}\nabla G(\mathbf{x},t)\right) = \delta(t)\delta\left(\mathbf{x}-\mathbf{x}_s\right), \tag{13}$$

where $v(\mathbf{x})$ is the velocity, $\rho(\mathbf{x})$ is the density, and $\delta()$ is the Kronecker delta function. Because it is difficult to estimate density accurately using seismic data, we consider only the high-wavenumber velocity perturbations as the reflectivity model in LSM. Based on the Born approximation (Aki & Richards, 1980), the velocity and data can be linearized as

$$\begin{aligned} v(\mathbf{x}) &= v_0(\mathbf{x}) + v_1(\mathbf{x}),\\ d\left(\mathbf{x}_r;\mathbf{x}_s,t\right) &= d_0\left(\mathbf{x}_r;\mathbf{x}_s,t\right) + d_1\left(\mathbf{x}_r;\mathbf{x}_s,t\right), \end{aligned} \tag{14}$$

where subscripts 0 and 1 denote the background and perturbed arguments. Inserting Equation 14 into Equation 12, we obtain the perturbed data as

$$d_1\left(\mathbf{x}_r;\mathbf{x}_s,t\right) = 2\int_0^T\int_0^T\int_\Omega \frac{\partial^2 f\left(t'-t''\right)}{\partial t''^2}G\left(\mathbf{x};\mathbf{x}_s,t''\right)\frac{m_1(\mathbf{x})}{v_0^2(\mathbf{x})}G\left(\mathbf{x}_r;\mathbf{x},t-t'\right)d\mathbf{x}^3dt''dt', \tag{15}$$

where Ω denotes the subsurface image domain of interest. $m_1(\mathbf{x})$ is the reflectivity model and it is defined as the relative velocity perturbation:

$$m_1(\mathbf{x}) = \frac{v_1(\mathbf{x})}{v_0(\mathbf{x})}. \tag{16}$$

Then, the Hessian can be expressed as the second-order derivative of the misfit function in Equation 4, which yields

$$H(\mathbf{x},\mathbf{y}) = \frac{\partial J^2(r)}{\partial m_1(\mathbf{x})\partial m_1(\mathbf{y})} = \left[\frac{\partial d_1(r)}{\partial m_1(\mathbf{x})}\right]^\dagger\frac{\partial d_1(r)}{\partial m_1(\mathbf{y})}. \tag{17}$$

Substituting d_1 in Equation 17 with Equation 15, we have

$$H(\mathbf{x},\mathbf{y}) = \frac{4}{v_0^2(\mathbf{x})v_0^2(\mathbf{y})} \sum_{\mathbf{x}_s,\mathbf{x}_r} \int_0^T \int_0^T \int_0^T \frac{\partial^2 f(t'-t'')}{\partial t''^2} G(\mathbf{x};\mathbf{x}_s,t'') G(\mathbf{x}_r;\mathbf{x},t-t') dt'' dt' \times \int_0^T \int_0^T \frac{\partial^2 f(t'-t'')}{\partial t''^2} G(\mathbf{y};\mathbf{x}_s,t'') G(\mathbf{x}_r;\mathbf{y},t-t') dt'' dt' dt, \quad (18)$$

Equation 18 indicates that the Hessian elements can be calculated in the following two ways. One is to compute perturbed data $d_1(\mathbf{x}_r;\mathbf{x}_s,t)$ from point scatterers at $\mathbf{x}$ and $\mathbf{y}$ over all sources and receivers separately, and then apply a dot product of these two data sets. The other way is to first compute perturbed data $d_1(\mathbf{x}_r;\mathbf{x}_s,t)$ from a point scatterer at $\mathbf{x}$, and then migrate these records to location $\mathbf{y}$. Both methods require calculating four Green's functions in modeling or migration.

The PSF is the migration response of a point scatterer under a given acquisition geometry and background velocity model. It is equivalent to the image calculated by mapping one column of the Hessian matrix to the image domain. As analyzed by Tang (2009) and Yang et al. (2021), with a good source and receiver coverage, the PSFs are spatially local functions with concentrated energy in the vicinity of point scatterers. Therefore, based on the Hessian in Equation 18, we can write the PSF as

$$P_{sf}(\mathbf{x},\mathbf{h}) = \frac{2}{v_0^2(\mathbf{x}+\mathbf{h})} \sum_{\mathbf{x}_s,\mathbf{x}_r} \int_0^T \int_0^T \frac{\partial^2 f(t'-t'')}{\partial t''^2} G(\mathbf{x}+\mathbf{h};\mathbf{x}_s,t'') dt'' \times \int_0^T G(\mathbf{x}+\mathbf{h};\mathbf{x}_r,t-t') d_{ps}(\mathbf{x}_r;\mathbf{x};\mathbf{x}_s,t) dt dt', \quad (19)$$

for the data generated from a point scatterer at $\mathbf{x}$

$$d_{ps}(\mathbf{x}_r;\mathbf{x};\mathbf{x}_s,t) = \frac{2}{v_0^2(\mathbf{x})} \int_0^T \int_0^T \int_\Omega \frac{\partial^2 f(t'-t'')}{\partial t''^2} G(\mathbf{x};\mathbf{x}_s,t'') \delta(\mathbf{x}'-\mathbf{x}) G(\mathbf{x}_r;\mathbf{x},t-t') d\mathbf{x}'^3 dt'' dt', \quad (20)$$

where $\mathbf{x}$ denotes the point scatterer location and $\mathbf{h}$ is the subsurface offset vector. In this study, we set the subsurface offset as $|h_i| < 2\lambda_{\max}(i = x, y, z)$ (the detailed analysis for this choice is given in Appendix A), where is $\lambda_{\max}$ is the maximum wavelength. Yang et al. (2021) derived the analytical expression of the Hessian and verified that with good source and receiver coverage, the PSFs are focused in a limited region around their center $\mathbf{x}$. Thus, we compute the PSFs in Equation 19 by migrating data $d_{ps}(\mathbf{x}_r;\mathbf{x};\mathbf{x}_s,t)$ to a small subsurface volume around $\mathbf{x}$. This helps to reduce the number of cross-correlations in adjoint migration compared with the Hessian calculation using Equation 18 (Valenciano et al., 2006).

2.3. An Efficient Method to Calculate the PSFs

As one of the advanced ray-based method, the Gaussian beams, have stable amplitudes near the caustic surface and can easily handle multipath arrivals (Červený et al., 1982; Hill, 1990, 2001). In addition, it can be used to efficiently do demigration and remigration for subsurface scatterers independently. Here, we utilize the Gaussian beam propagator to compute the Green's function (the details can be found in Appendix B). Then, the PSF in Equation 19 can be reformulated as

$$P_{sf}(\mathbf{x},\mathbf{h}) = \frac{2}{v_0^2(\mathbf{x}+\mathbf{h})} \sum_{\mathbf{x}_s,\mathbf{x}_r} \int_0^T dt \iint \frac{dp_x^s dp_y^s}{p_z^s} \iint \frac{dp_x^r dp_y^r}{p_z^r} \mathrm{Re}\left[A^*(\mathbf{x}_r;\mathbf{x}+\mathbf{h};\mathbf{x}_s) \times d_{fps}(\mathbf{x}_r;\mathbf{x};\mathbf{x}_s,T_i(\mathbf{x}_r;\mathbf{x}+\mathbf{h};\mathbf{x}_s),t+T_r(\mathbf{x}_r;\mathbf{x}+\mathbf{h};\mathbf{x}_s))\right], \quad (21)$$

where * denotes the complex conjugate, p_x, p_y, and p_z are the components of the ray parameter, superscript s and r denote source-side and receiver-side variables, $A(\mathbf{x}_r;\mathbf{x};\mathbf{x}_s)$ is the complex-valued two-way amplitude, $T_r(\mathbf{x}_r;\mathbf{x};\mathbf{x}_s)$ and $T_i(\mathbf{x}_r;\mathbf{x};\mathbf{x}_s)$ are the real and imaginary parts of the two-way travel time T. $d_{fps}(\mathbf{x}_r;\mathbf{x};\mathbf{x}_s,Ti,t)$ is the filtered point-scatterer response

$$d_{fps}(\mathbf{x}_r;\mathbf{x}_s,Ti,t) = \int_{-\infty}^{+\infty} \frac{\omega^4}{4\pi^2} F^*(\omega)\exp(i\omega t - \omega T_i) D_{ps}(\mathbf{x}_r;\mathbf{x};\mathbf{x}_s,\omega) d\omega, \quad (22)$$

where $D_{ps}(\mathbf{x}_r;\mathbf{x};\mathbf{x}_s,\omega)$ is the spectrum of the data $d_{ps}(\mathbf{x}_r;\mathbf{x};\mathbf{x}_s,t)$, which can be computed as

$$d_{ps}\left(\mathbf{x}_r;\mathbf{x};\mathbf{x}_s,t\right)=\frac{2}{v_0^2(\mathbf{x})}\iint\frac{dp_x^s dp_y^s}{p_z^s}\iint\frac{dp_x^r dp_y^r}{p_z^r}\int_\Omega d\mathbf{x}'^3\delta\left(\mathbf{x}'-\mathbf{x}\right)\times\mathrm{Re}\left[A\left(\mathbf{x}_r;\mathbf{x};\mathbf{x}_s\right)f'\left(T_i\left(\mathbf{x}_r;\mathbf{x};\mathbf{x}_s\right),t-T_r\left(\mathbf{x}_r;\mathbf{x};\mathbf{x}_s\right)\right)\right],\tag{23}$$

with a filtered source wavelet $f'(T_i, t)$ as

$$f'(T_i,t)=\int_{-\infty}^{+\infty}\frac{\omega^4}{4\pi^2}F(\omega)\exp\left(i\omega t-\omega T_i\right)d\omega,\tag{24}$$

and $F(\omega)$ is the Fourier transform of a source time function.

The common-source data generated from a subsurface point scatterer is usually one hyperbolic event, or a few events because of multipath arrivals in complicated structures. To reduce memory and computation cost, we only calculate and store the records $d_{ps}(\mathbf{x}_r; \mathbf{x}; \mathbf{x}_s, t)$ and $d_{fps}(\mathbf{x}_r; \mathbf{x}; \mathbf{x}_s, T_i, t)$ in a short time window. This enables us to simplify the PSF in Equation 21 as

$$P_{sf}(\mathbf{x},\mathbf{h})=\frac{2}{v_0^2(\mathbf{x}+\mathbf{h})}\sum_{\mathbf{x}_s,\mathbf{x}_r}\int_{t_0-\Delta t}^{t_0+\Delta t}dt\iint\frac{dp_x^s dp_y^s}{p_z^s}\iint\frac{dp_x^r dp_y^r}{p_z^r}\mathrm{Re}\left[A^*\left(\mathbf{x}_r;\mathbf{x}+\mathbf{h};\mathbf{x}_s\right)\times d_{fps}\left(\mathbf{x}_r;\mathbf{x};\mathbf{x}_s,Ti\left(\mathbf{x}_r;\mathbf{x}+\mathbf{h};\mathbf{x}_s\right),t+T_r\left(\mathbf{x}_r;\mathbf{x}+\mathbf{h};\mathbf{x}_s\right)-t_0\right)\right],\tag{25}$$

where t_0 is the reference travel time and can be precomputed using ray tracing, Δt is the half time window and is set to two periods of the wavelet. The localized features in both time ($|t-t_0|\le\Delta t$) and space ($|\mathbf{y}-\mathbf{x}|\le h_{\max}$) for computing the PSFs using Equation 25 enables us to significantly reduce the cost in comparison with directly computing the Hessian, where $h_{\max}$ is the maximum subsurface offset. Since the PSFs are calculated independently for subsurface locations, the cost is proportional to its number. To save computational cost while capturing the PSF variations caused by velocity contrast, we compute PSFs on a coarse grid with a spacing five to eight times of the fine image grid increment. In addition, the local plane-wave decomposition in Gaussian beam migration proposed by Hill (1990) is adopted to further reduce the number of Green's function calculations. The detailed expression can be found in Hill (1990, 2001). In the beam method, the ray tracing results are commonly stored in the memory and can be repeatedly used for computing the Green's function. These optimizations make it possible to efficiently calculate the Hessian matrix for large-scale problems.

2.4. PSF Deconvolution

In this section, we apply a multidimensional PSF deconvolution to traditional adjoint migration results in the wavenumber domain to reduce Hessian blurring effects and compensate for deep amplitudes. To attenuate artifacts far away from the PSF center, we apply a weighting function to the PSFs as

$$P_{sfw}(\mathbf{x},\mathbf{h})=\frac{1}{\left(\sqrt{2\pi}\sigma\right)^3}\exp\left(-\frac{1}{2}\frac{|\mathbf{h}|^2}{\sigma^2}\right)P_{sf}(\mathbf{x},\mathbf{h}),\tag{26}$$

where $P_{sf}(\mathbf{x}, \mathbf{h})$ is the PSF calculated using Equation 25, $P_{sfw}(\mathbf{x}, \mathbf{h})$ is the weighted PSF, $\mathbf{h}$ denotes the subsurface offset in the PSF window, σ is the standard deviation of the weighting function and we set it to one-third of the maximum subsurface offset in this study.

The multidimensional partitions of unity (Bale et al., 2002) can be expressed as

$$1\equiv\sum_{\mathbf{x}}\frac{\Delta x\Delta y\Delta z}{\left(\sqrt{2\pi}\sigma\right)^3}\exp\left(-\frac{1}{2}\frac{|\mathbf{y}-\mathbf{x}|^2}{\sigma^2}\right),\tag{27}$$

where $\mathbf{x}$ denotes the PSF center location, $\mathbf{y}$ is another spatial variable as in Equation 18, and Δx, Δy, and Δz are the spacings between PSF centers along different directions. Using the partition in Equation 27, we decompose the migration result into local images as

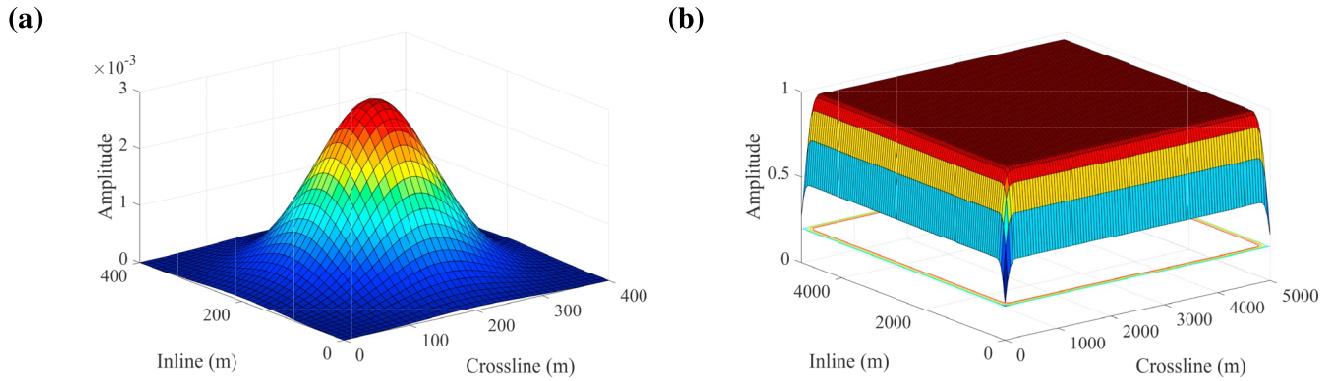

Figure 1. An example of 2D partition of unity using Gaussian functions. (a) A Gaussian function with the standard deviation of 100 m, and (b) the approximated unit using the Gaussian function summation.

$$I_{local}(\mathbf{x},\mathbf{y}) = I(\mathbf{y})\frac{\Delta x\Delta y\Delta z}{\left(\sqrt{2\pi}\sigma\right)^3}\exp\left(-\frac{1}{2}\frac{(\mathbf{y}-\mathbf{x})^2}{\sigma^2}\right), \tag{28}$$

where $I(\mathbf{y})$ is the entire image volume computed using traditional adjoint migration. Figure 1 illustrates an example for 2D partition of unity. With sufficient sampling for the PSF scenters, the unit can be well approximated by the sum of Gaussian functions in the main area, and has some errors near boundaries. Considering extremely small amplitudes outside the Gaussian window ($|\mathbf{y}-\mathbf{x}| > h_{\max}$), we express $\mathbf{y} = \mathbf{x} + \mathbf{h}$ and rewrite Equation 28 as

$$I_{local}(\mathbf{x},\mathbf{h}) = I(\mathbf{x}+\mathbf{h})\frac{\Delta x\Delta y\Delta z}{\left(\sqrt{2\pi}\sigma\right)^3}\exp\left(-\frac{1}{2}\frac{|\mathbf{h}|^2}{\sigma^2}\right), \tag{29}$$

Then, we deconvolve these local images by the weighted PSFs in Equation 26 and assemble the deconvolved local images as

$$I_{decon}(\mathbf{x}) = \sum_{\mathbf{h}}\frac{\Delta x\Delta y\Delta z}{\left(\sqrt{2\pi}\sigma\right)^3}\exp\left(-\frac{1}{2}\frac{|\mathbf{h}|^2}{\sigma^2}\right)\mathcal{F}_{\mathbf{h}}^{-1}\left[\frac{\mathcal{F}_{\mathbf{h}}\left[I_{local}(\mathbf{x},\mathbf{h})\right]}{\mathcal{F}_{\mathbf{h}}\left[P_{sfw}(\mathbf{x},\mathbf{h})\right]+\epsilon(\mathbf{x})}\right], \tag{30}$$

where $\mathcal{F}_{\mathbf{h}}$ is the multidimensional Fourier transform for subsurface offsets and $\mathcal{F}_{\mathbf{h}}^{-1}$ is the corresponding inverse transform. $\epsilon(\mathbf{x})$ is a spatially varying function to avoid division by zero, which is computed by first setting it to one thousandth of the maximum wavenumber spectrum of $P_{sfw}(\mathbf{x},\mathbf{h})$ and then applying a spatial smoothing function.

According to the above descriptions for the PSF calculation and deconvolution, the proposed imaging scheme can be summarized as follows:

1. Computing the PSFs $P_{sf}(\mathbf{x},\mathbf{h})$ using Equation 25 on a coarse grid, where the grid spacing is set as five to eight times of the fine image increment to sufficiently capture the PSF variations associated with model heterogeneities.
2. Calculating the image $I(\mathbf{x})$ using traditional adjoint migration and decomposing it to local images $I_{local}(\mathbf{x},\mathbf{h})$ according to Equation 29.
3. Computing the PSFs on a fine image grid using bilinear interpolation and weighting the PSFs using a multidimensional Gaussian function according to Equation 26 to attenuate artifacts that are far from the PSF centers.
4. Applying PSF deconvolution and the inverse of multidimensional unit partitions according to Equation 30 to reconstruct the deconvolved image $I_{decon}(\mathbf{x})$.

In numerical implementation, the PSF interpolation on a fine grid is performed on the fly during the multidimensional deconvolution. Thus, it is not necessary to store the PSFs of the fine grids in memory or disk, and thus with small storage cost.

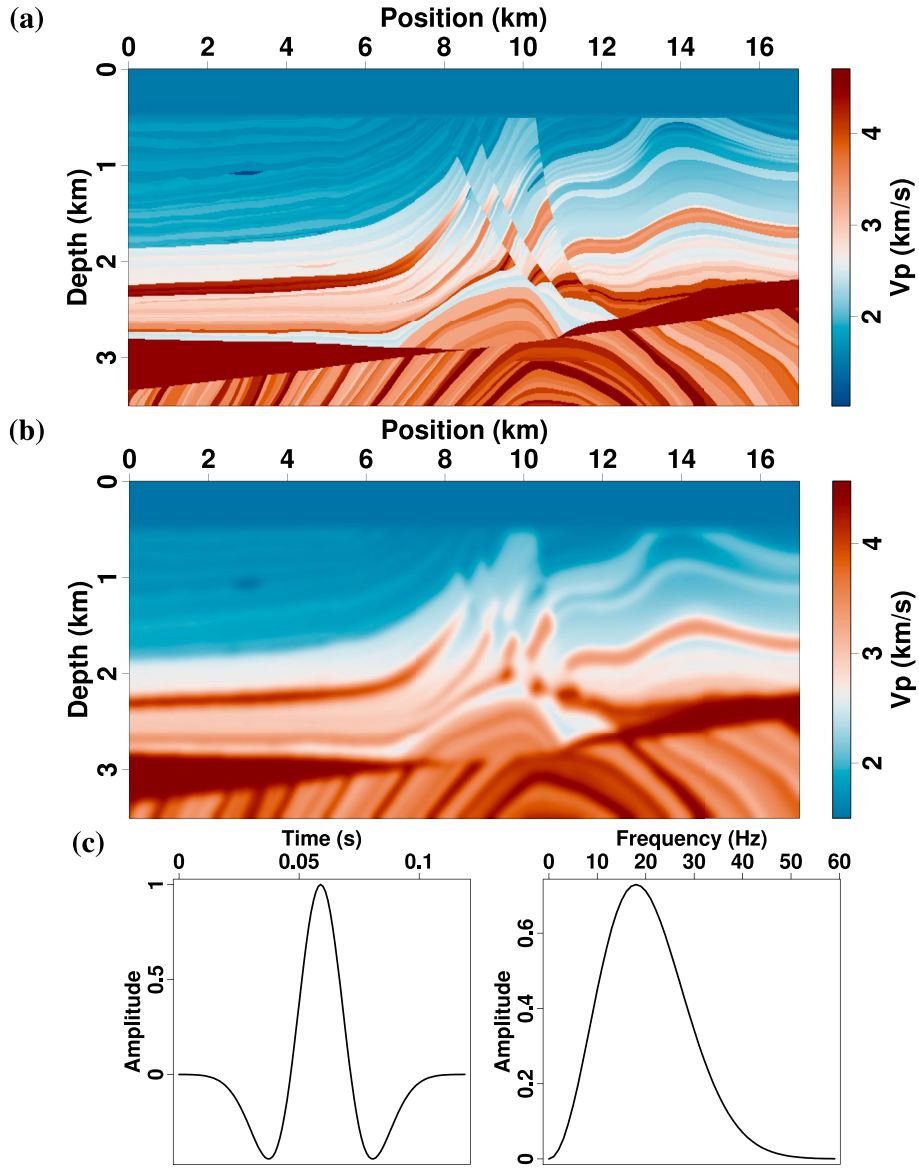

Figure 2. The Marmousi benchmark model. (a) True velocity model, (b) smoothed migration velocity model, (c) wavelet (left) and its spectrum (right) used in modeling and migration.

3. Numerical Examples

In this section, two benchmark models and one field data set from a land survey are used to test the performance of the proposed PSF deconvolution approach. Observed data for these benchmark models are calculated using full-waveform modeling with a staggered-grid finite-difference algorithm. In the comparison of migration results, we also compute adjoint migration and data-domain LSM results, which are all implemented using the Gaussian beam propagator. In data-domain LSM, the Tikhonov regularization is applied to reduce the overfitting artifacts for noise and improve the inversion stability.

3.1. Marmousi Model

The benchmark Marmousi model (Bourgeois et al., 1990) is shown in Figure 2a, which is discretized on a $351 \times 2{,}101$ grid with a 10-m increment. The migration velocity model (Figure 2b) is calculated by applying a Gaussian smoother to the true model. Observed data (Figure 3) has 165 sources, which are evenly distributed

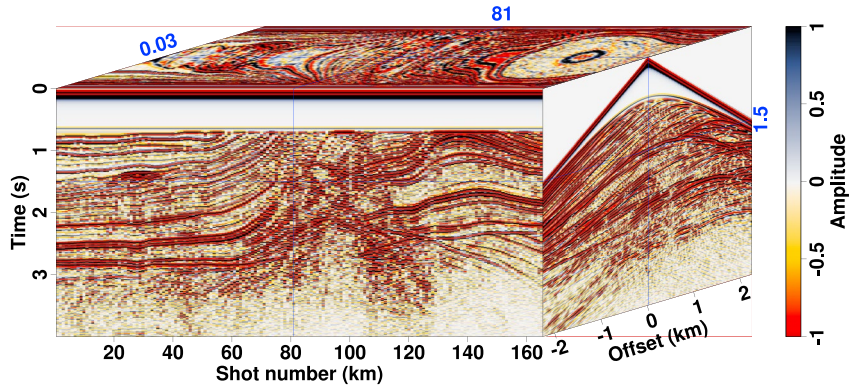

Figure 3. Common-shot data of Marmousi model computed using the full-waveform modeling with a time-domain staggered-grid finite-difference method.

on the surface. Each source is recorded by 451 receivers within a 4.5-km aperture. The source time function is a Ricker wavelet with a dominant frequency of 18 Hz (Figure 2c), and direct waves are muted before migration.

Representative PSFs in Figure 4 are calculated on a coarse grid with a spacing six times that of the fine image grid. The complicated structures of the Marmousi model result in spatially varying PSFs. Uniform illumination at shallow depths produces focused PSFs with good horizontal and vertical resolution. As the depth increases, the PSFs show a vertically elongated pattern. This is because the deep reflectors are mainly resolved by small scattering angles due to limited offsets. In the complex fault zone, strong velocity variations and irregular illumination lead to distorted PSFs, which are asymmetric and have long tails. In the bottom anticline, the PSFs have weak amplitudes and structure-oriented distortions. An example of the PSF deconvolution at the location of $x = 7.05$ km and $z = 2.12$ km is illustrated in Figure 5. Compared with the original image, the deconvolved image has a more focused peak lobe, reduced side lobes, and broader effective wavenumber range, suggesting improved spatial resolution.

Comparisons of the true reflectivity model with three migration results, i.e., traditional adjoint migration, data-domain LSM, and the proposed PSF deconvolution, are presented in Figure 6. The true reflectivity (Figure 6a) is calculated as $r = \frac{v - v_0}{v_0}$ and we use it as a reference in following comparisons, where v denotes the true model and v_0 denotes the smoothed model. We use the local similarity (Figure 7) between the true reflectivity model with migration results to quantitatively evaluate the imaging quality. Although basic structures have been imaged by adjoint migration, the finite-frequency effect and irregular illumination yield relatively low

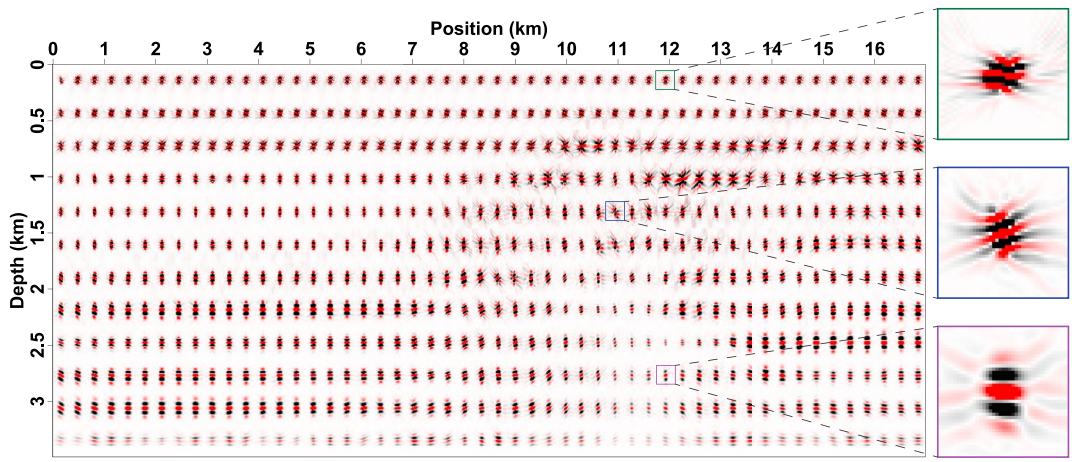

Figure 4. The point-spread functions (PSFs) for the Marmousi model computed using the propose method. Every 10 PSFs are shown in the main panel on the coarse grid. The right insets are three enlarged PSFs plotted at a 1:1 scale in shallow, middle, and large depths, respectively.

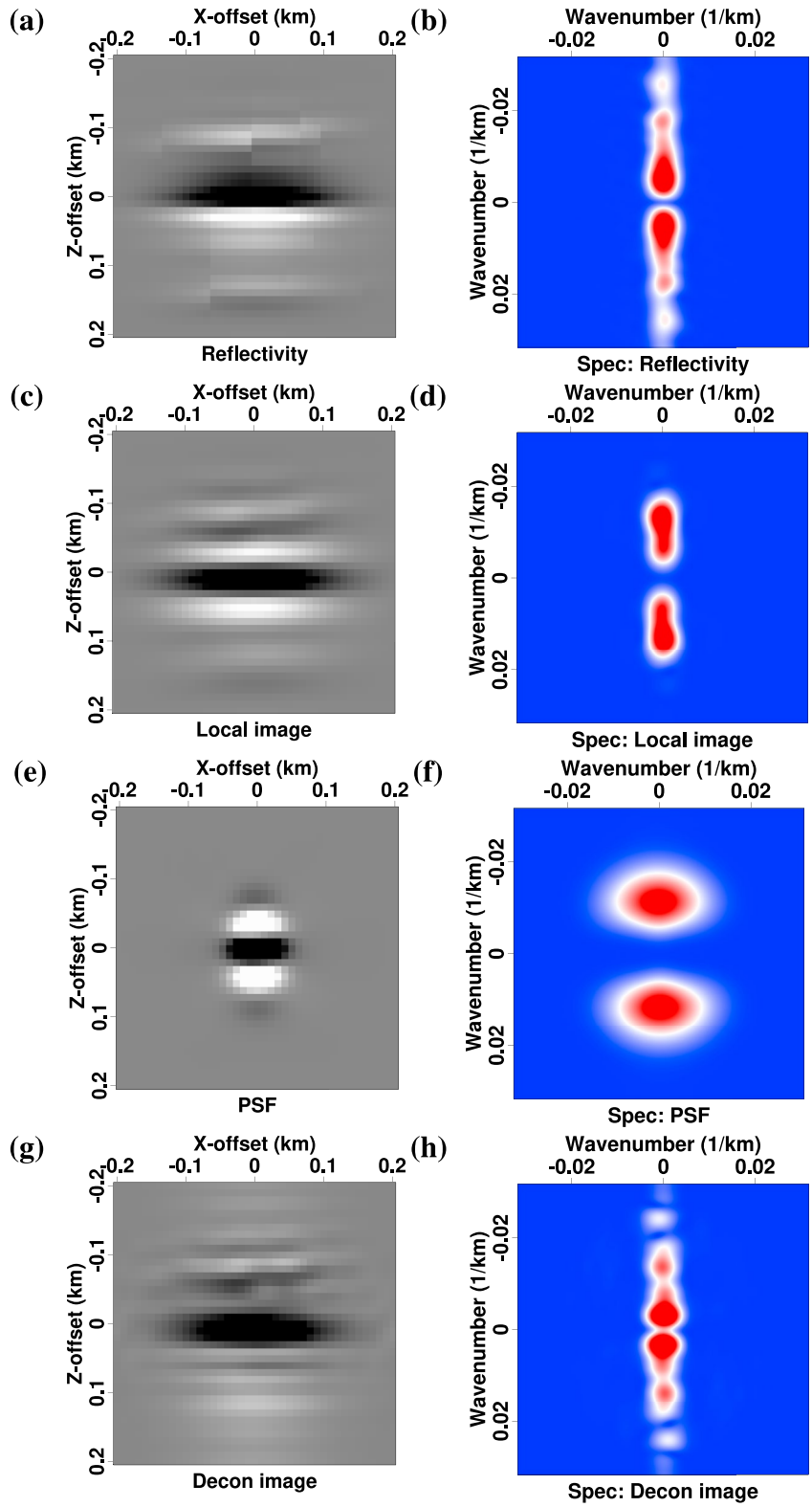

Figure 5. An example of the point-spread function (PSF) deconvolution at $x = 7.05$ km and $z = 2.12$ km for the Marmousi model. (a) True reflectivity, (c) local image, (e) PSF, (g) PSF deconvolution result. Panels (b), (d), (f), and (h) are the corresponding wavenumber spectra. The local images and PSF have been applied a Gaussian weighting function.

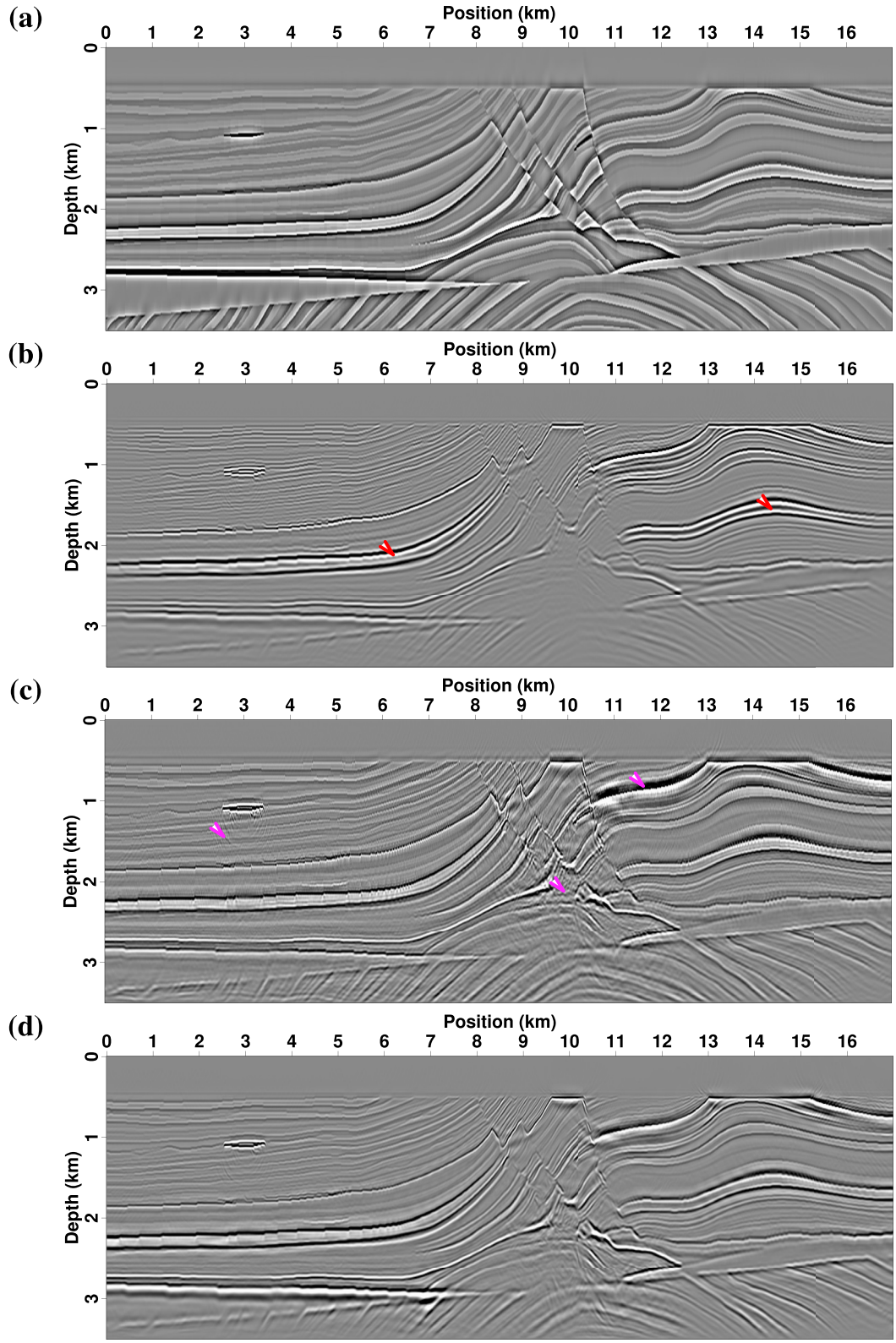

Figure 6. Comparison between the true reflectivity model with migration results of the Marmousi model. (a) True reflectivity model, (b) traditional adjoint migration, (c) data-domain least-squares migration (LSM) after 10 iterations, and (d) the proposed point-spread function (PSF) deconvolution.

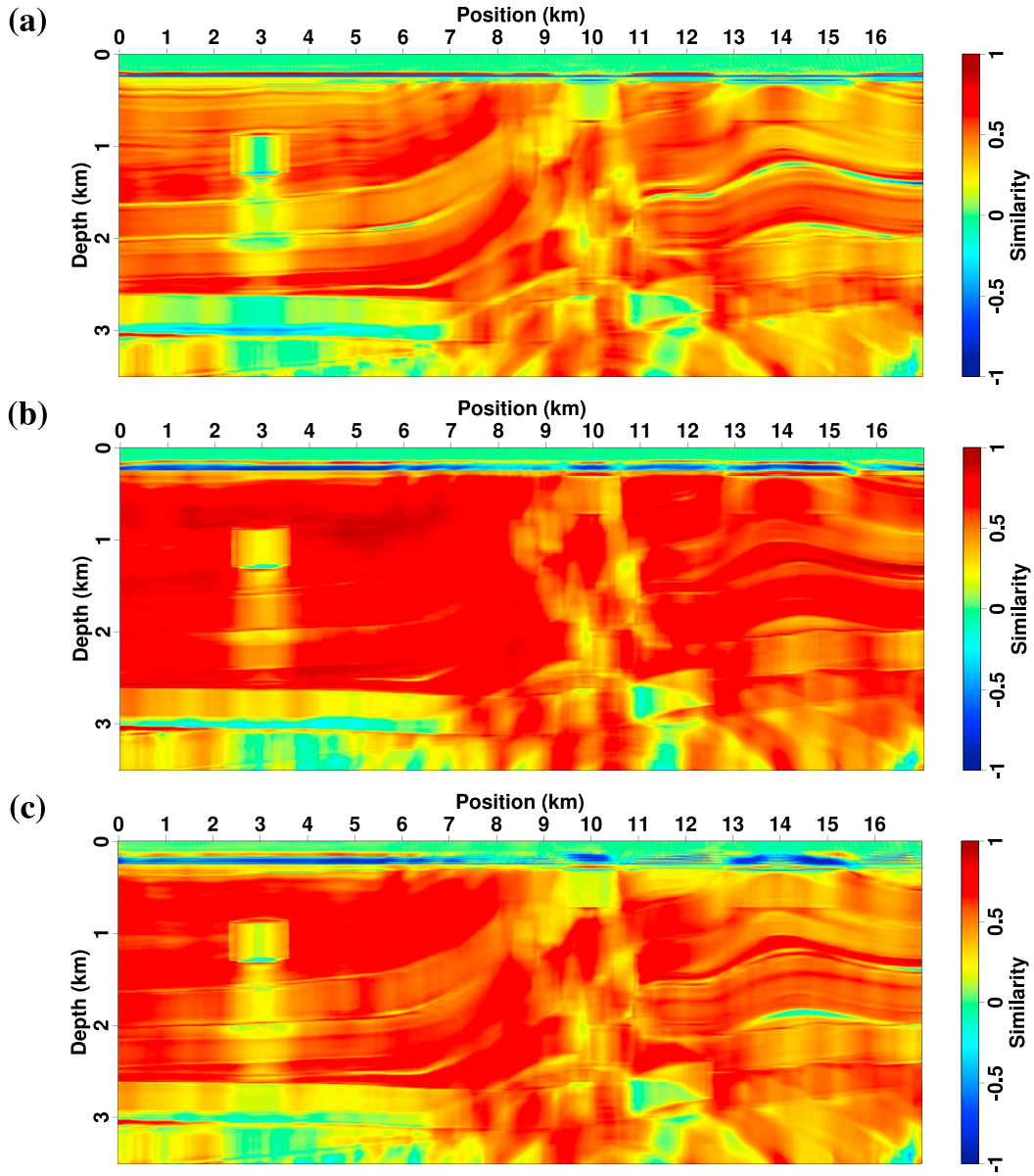

Figure 7. Similarity between migration results with the true reflectivity model of the Marmousi model. (a) Traditional adjoint migration, (b) data-domain least-squares migration (LSM), and (c) the proposed point-spread function (PSF) deconvolution.

resolution and weak amplitudes at the great depths. Neighboring strong reflectors (the red arrows in Figure 6b) are difficult to distinguish, and the reflectors from the bottom anticline are not continuous. By fitting observed data with Born modeling data, data-domain LSM incorporates the Hessian effects and significantly improves image resolution and structure similarity to true reflectivity model (Figures 6a, 6c, and 7b). The fault planes are recovered clearly, and the deep weak reflectors for the pinch-outs, anticline, and angular unconformity are imaged well. One drawback of data-domain LSM is that overfitting between observed and synthetic data might introduce strong high-wavenumber swing artifacts (the magenta arrows in Figure 6c), especially around fault corners and discontinuities. The proposed method computes an approximate Hessian using local PSFs and applies the PSF deconvolution, which enables significant improvement of image resolution compared with traditional adjoint migration (Figures 6d and 7c), while producing fewer swing artifacts than data-domain LSM.

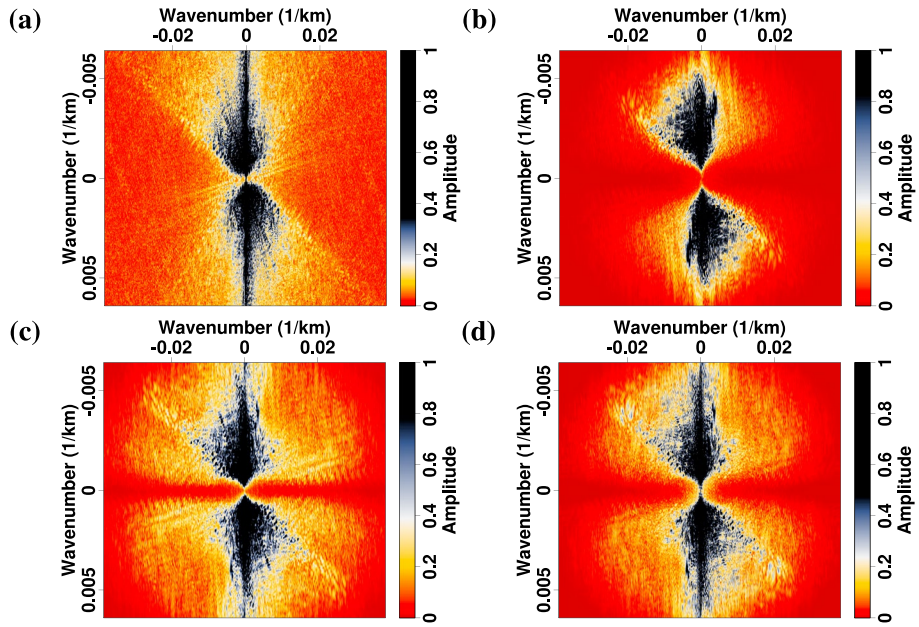

Figure 8. Comparisons of the wavenumber spectra between the true reflectivity model and migration results for the Marmousi model. (a) True reflectivity model, (b) traditional migration, (c) data-domain least-squares migration (LSM), and (d) the proposed point-spread function (PSF) deconvolution result.

Comparisons of wavenumber spectra (Figure 8) between the true reflectivity and the migration results reveal that because of the finite-frequency effect of the source wavelet, the adjoint migration produces a band-limited wavenumber spectrum. In contrast, data-domain LSM and PSF deconvolution expand the wavenumber spectrum to low and high wavenumber ends and produce similar spectral range to that of the true reflectivity model, indicating improved spatial resolution. In addition, the PSF deconvolution incorporate the diagonal Hessian effect, which helps to compensate for geometric spreading and unbalanced illumination, resulting in deep amplitudes comparable to the reference image (Figure 9).

3.2. Pluto Model

The benchmark Pluto model (Figure 10a) is built by Stoughton et al. (2001) according to a typical geological environment in the Gulf of Mexico, which includes complicated salt bodies, various faults, pinch-outs, and subsalt gas sand strata. The observed data set (Figure 10b) consists of 129 shots, which are uniformly deployed on the surface. Each common-source gather has 601 traces with an increment of 10 m. The migration velocity

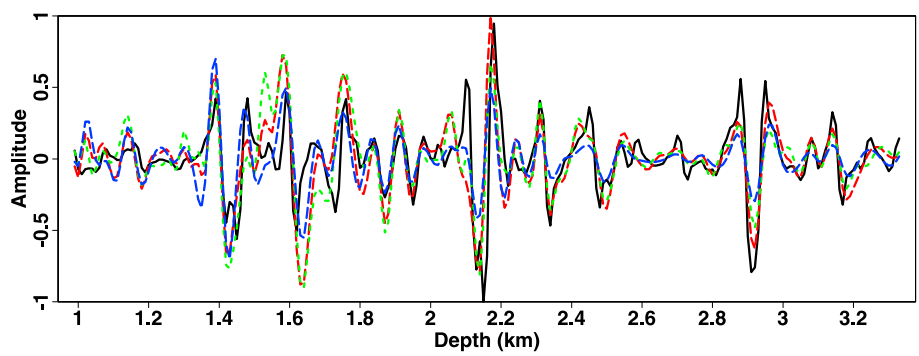

Figure 9. Comparisons of depth logs between the true reflectivity model with migration results at $x = 10$ km for the Marmousi model. The black solid line denotes the true reflectivity model, the blue dashed line is traditional migration result, the green dashed line is the data-domain least-squares migration (LSM) result, and (d) the red dashed line is the proposed point-spread function (PSF) deconvolution result.

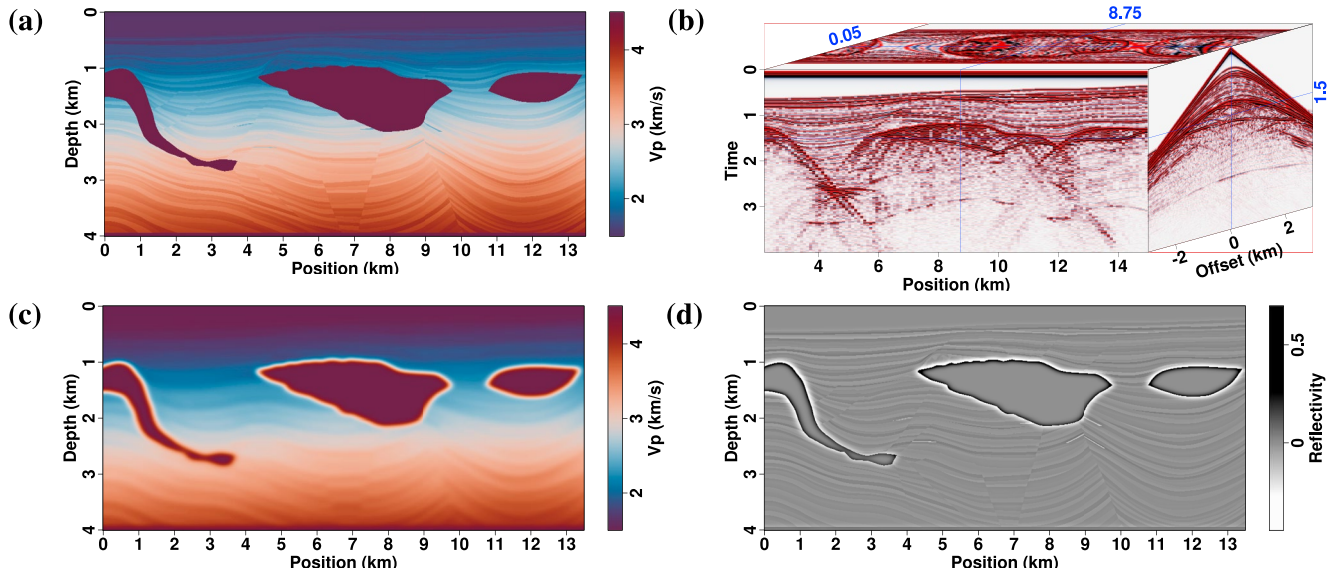

Figure 10. A benchmark Pluto salt model. (a) True velocity model, (b) common-source observed data, (c) smoothed migration velocity model, and (d) true reflectivity model.

model (Figure 10c) is computed by smoothing the true model with a Gaussian function of 50 m × 100 m. The true reflectivity model (Figure 10d) is computed as the relative velocity perturbation between the true and migration velocity models.

Representative PSFs calculated using the proposed method are presented in Figure 11. Since the Hessian strongly depends on the subsurface velocity distributions, the complex salt structure leads to different PSF patterns at different locations. For instance, above the salt domes, the shallow layers can be illuminated with good coverage over small and large scattering angles, which produces symmetrically focused PSFs. Inside the salt bodies, the high *P* wave velocity generates relatively wider PSFs than that within the sedimentary strata. In contrast, beneath the salt, unbalanced illumination, and low-fold zones (Figure 12a) result in weak amplitudes, strong side lobes, and rotated principal directions for PSFs. These distorted PSFs (the insets in Figure 11) indicate that subsalt migration results can be severely affected by complicated salt structures. The migration results using three

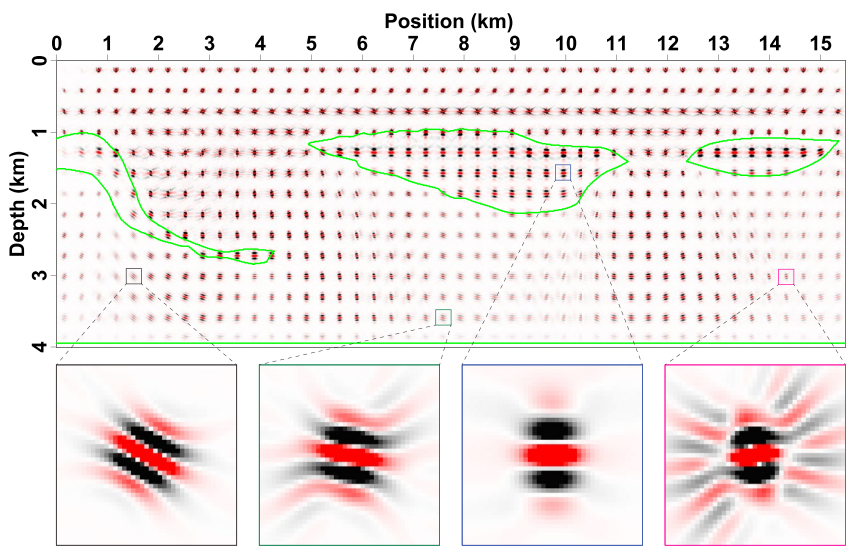

Figure 11. The point-spread functions (PSFs) for the Pluto salt model computed using the proposed method. The insets show the detailed PSFs at four different locations. The green lines denote the outlines of salt bodies.

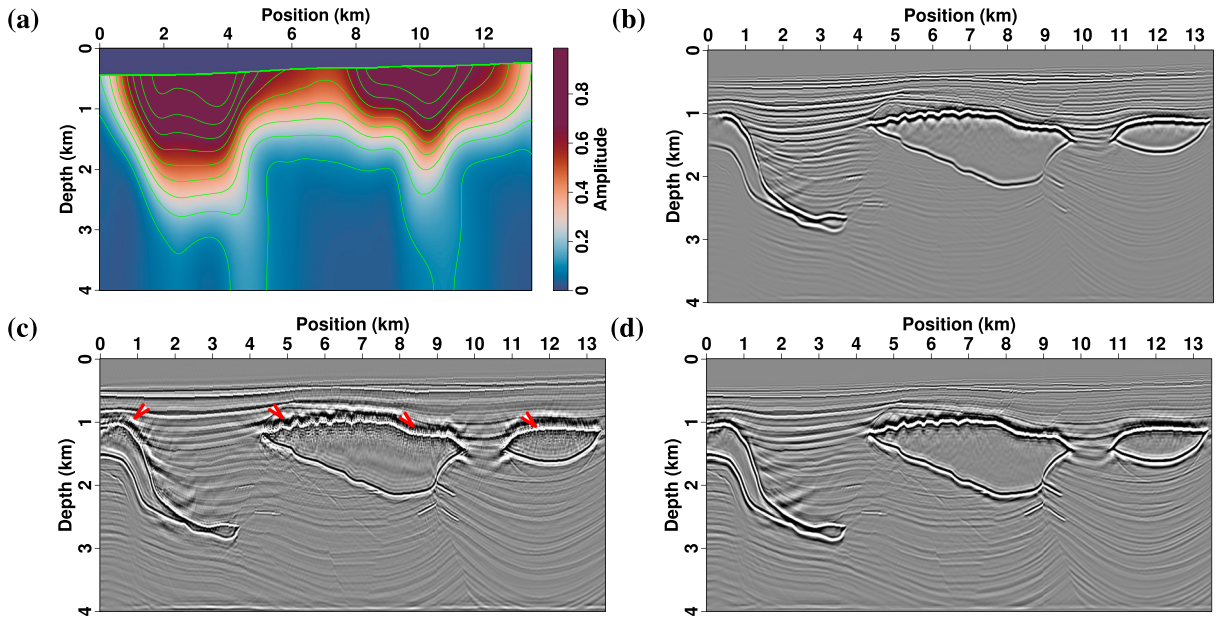

Figure 12. The diagonal Hessian and migration results for the Pluto model. (a) Diagonal Hessian, (b) adjoint migration result, (c) data-domain least-squares migration (LSM) result, and (d) the proposed point-spread function (PSF) deconvolution result. Blue lines in panel (a) are the contours of the diagonal Hessian.

different methods are shown in Figures 12b–12d, and enlarged views for a local region are presented in Figure 13. Traditional adjoint migration resolves shallow reflectors and top salt boundaries well, but produces weak amplitudes and low resolution at great depths (Figures 12b and 13b). By iteratively incorporating the Hessian effect, data-domain LSM significantly improves image quality for deep subsalt layers (Figures 12c and 13c). But the large amplitude differences between salt boundary and subsalt layers lead to unbalanced updates in LSM. With 10 iterations, the salt top reflections are over fitted while subsalt reflections are not well fitted. The data fitting

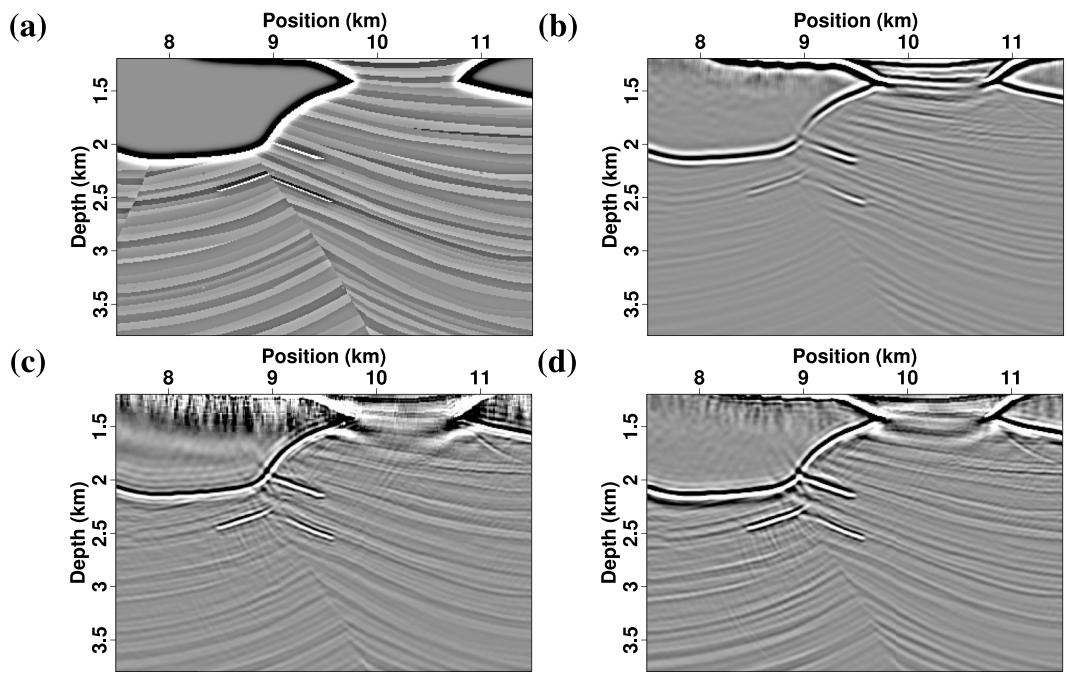

Figure 13. Enlarged local migration results for the Pluto model. (a) True reflectivity model, (b) adjoint migration result, (c) data-domain least-squares migration (LSM) result, and (d) the proposed point-spread function (PSF) deconvolution result.

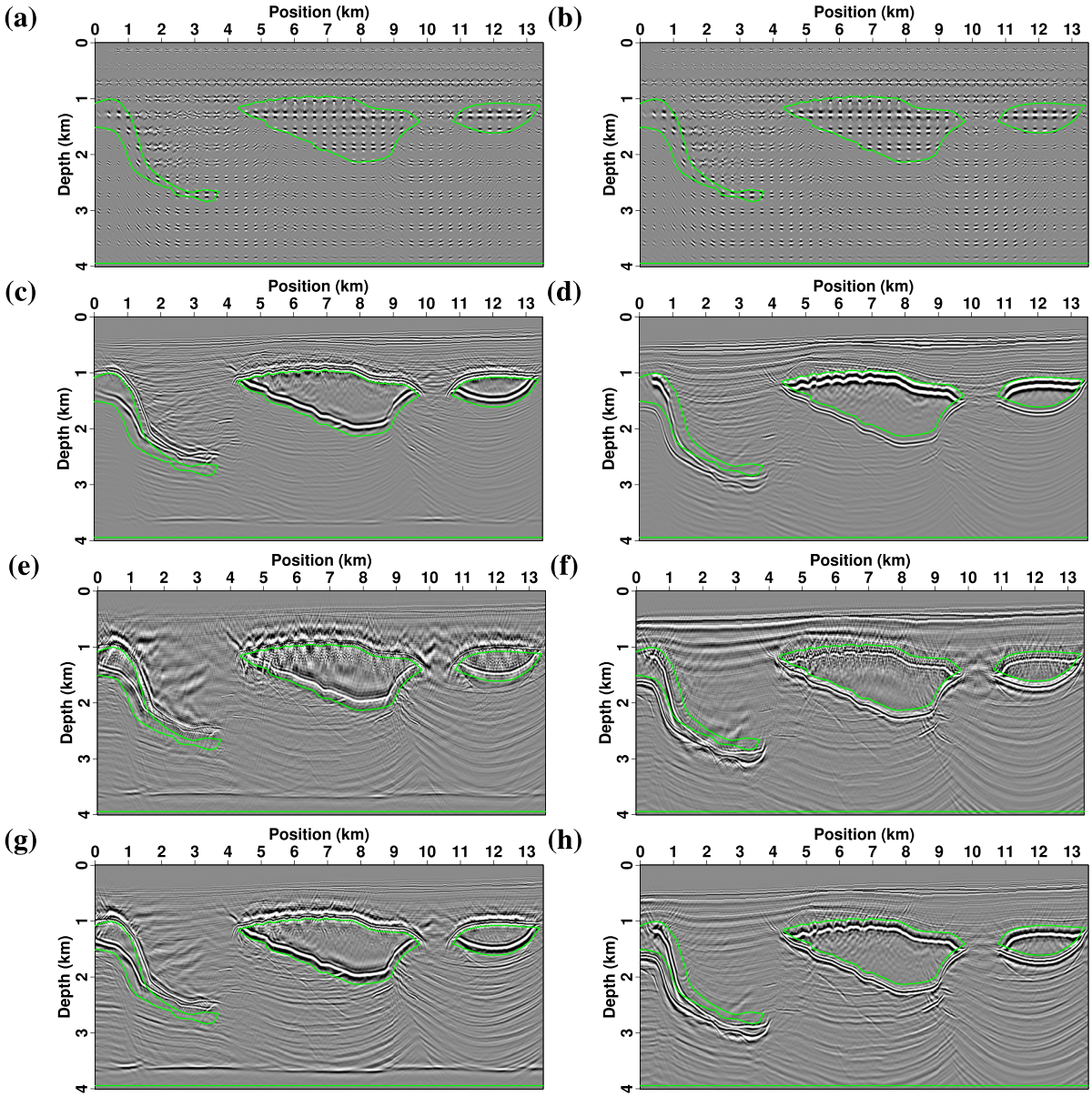

Figure 14. Point-spread functions (PSFs) and migration results using lower (left column) and higher (right column) velocity models. (a, b) PSFs, (c, d) adjoint migration results, (e, f) data-domain least-squares migration (LSM) results, and (g, h) the proposed PSF deconvolution results. The green solid lines denote the boundaries of salt bodies.

for large-amplitude salt reflections produces strong artifacts near salt flanks, which contaminate neighboring fine reflectors (the red arrows in Figure 12c). The proposed PSF deconvolution produces a high-quality image with good resolution and enhanced deep amplitudes (Figure 12d). Subsalt sedimentary reflectors, pinch-outs, and faults can be clearly identified. More importantly, it does not generate swing artifacts associated with large velocity contrasts and produces clear salt boundaries (Figure 13d).

To test the sensitivity of the PSF deconvolution to velocity errors, we design four inaccurate velocity models. The first two are constructed by multiplying the smoothed model in Figure 10c with 0.9 and 1.1, respectively. The corresponding PSFs and migration results are shown in Figure 14. Because the inaccurate velocity models are used in local modeling and migration, higher or lower velocity errors do not have large influences on the shapes of the PSFs (Figures 14a and 14b). Although subsurface reflectors are not imaged to correct positions by adjoint migration, basic structures, including salt outlines and subsalt layers, can still be clearly identified (Figures 14c

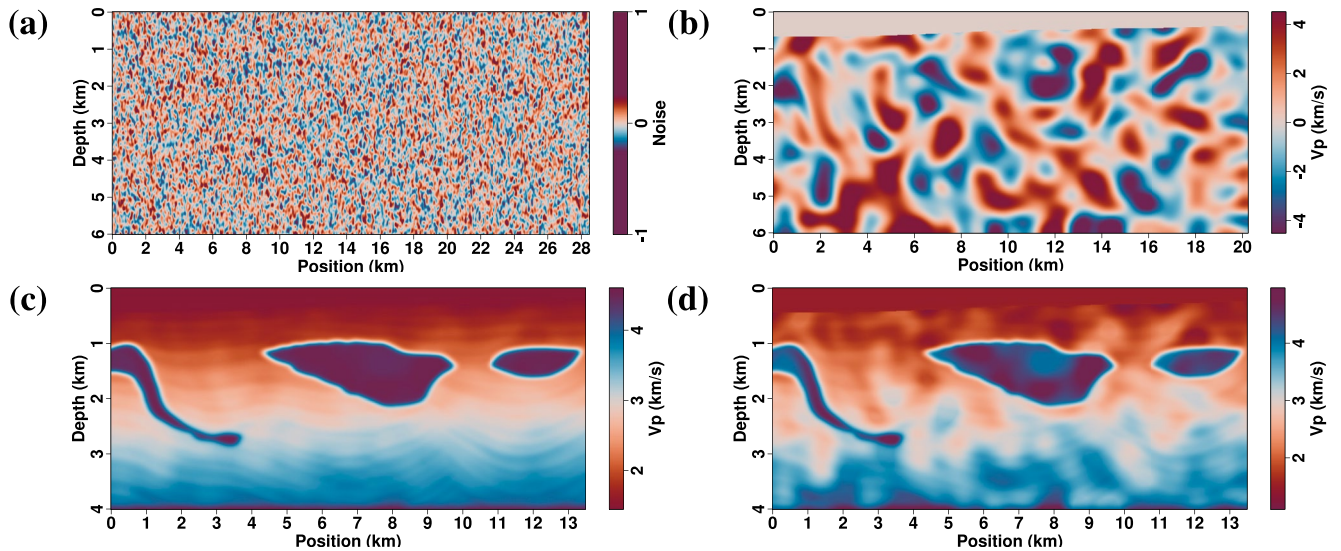

Figure 15. Inaccurate velocities with high-wavenumber perturbations for the Pluto salt model. (a) Bandpassed random noise, (b) smoothed velocity perturbations, and (c, d) migration velocity models with 2% and 10% perturbations.

and 14d). Because data fitting is very sensitive to velocity errors, data-domain LSM produces much worse results than adjoint migration. Both shallow fine layers and top salt boundaries are contaminated by swing artifacts, and deep subsalt reflectors are smeared (Figures 14e and 14f). Compared to the adjoint migration result, the proposed PSF deconvolution improves spatial resolution and enhances deep amplitudes, and does not introduce additional artifacts (Figures 14g and 14h). This indicates that PSF deconvolution has the same sensitivity as adjoint migration to velocity errors, but it is not as sensitive as data-domain LSM.

The other two inaccurate velocity models are built as follows. First, we generate a random noise image and apply a bandpass filter (Figure 15a). Then, a structural smoothing filter is used to generate realistic velocity perturbations v_{per}, followed by adding a mask for the water layer (Figure 15b). Finally, we add the high-wavenumber perturbations v_{per} to the smoothed migration velocity model v_0 as $v_{err} = v_0 + \kappa v_{per} \frac{\max(v_0)}{\max(v_{per})}$, where κ is a scaling factor and max denotes the maximum value. We choose κ as 0.02 and 0.1 to generate two inaccurate velocity models as shown in Figures 15c and 15d, and the corresponding migration results are presented in Figure 16. Like the results in Figure 14, the two different inaccurate velocity models have no significant effects on the overall PSF patterns (Figures 16a and 16b). Data-domain LSMs appear to be very sensitive to velocity errors, and produce strong migration noise (Figures 16e and 16f). The PSF deconvolutions (Figures 16g and 16h) have the same sensitivity, as traditional adjoint migration, to velocity errors. But when the velocity error increases to 10%, none of three methods can accurately recover deep subsalt structures (see the red arrows in Figure 16).

3.3. A Land Survey

The final example is for a field data from a land survey, which consists of 234 common-source gathers (Figure 17a). Two hundred and forty receivers are used for recording vertical particle velocities for each shot with an average 40-m spacing. Preprocessing for the field data includes killing of bad traces, surface wave attenuation, and direct wave muting. The migration velocity model (Figure 17b) is computed using ray-based tomography. The source wavelet is extracted according to the near-offset direct waves.

Representative PSFs are shown in Figure 18 and different migration results are presented in Figures 19 and 20. Because the velocity model has no strong variations, most PSFs appear to be regular and focused (Figure 18a), except for varying amplitudes associated with nonuniform illumination (Figure 18b). Although the prestack data have low signal-to-noise ratio (Figure 17a), adjoint migration produces clear reflectors for the shallow sedimentary layers and deeper buried hill structures after multifold stacking (Figures 19a, 20a, and 20b). For comparison, we apply the data-domain LSM and perform eight iterations. The resulting image has improved deep amplitudes and thinner reflection events. But the LSM introduces many side lobes near the true reflectors, especially in areas

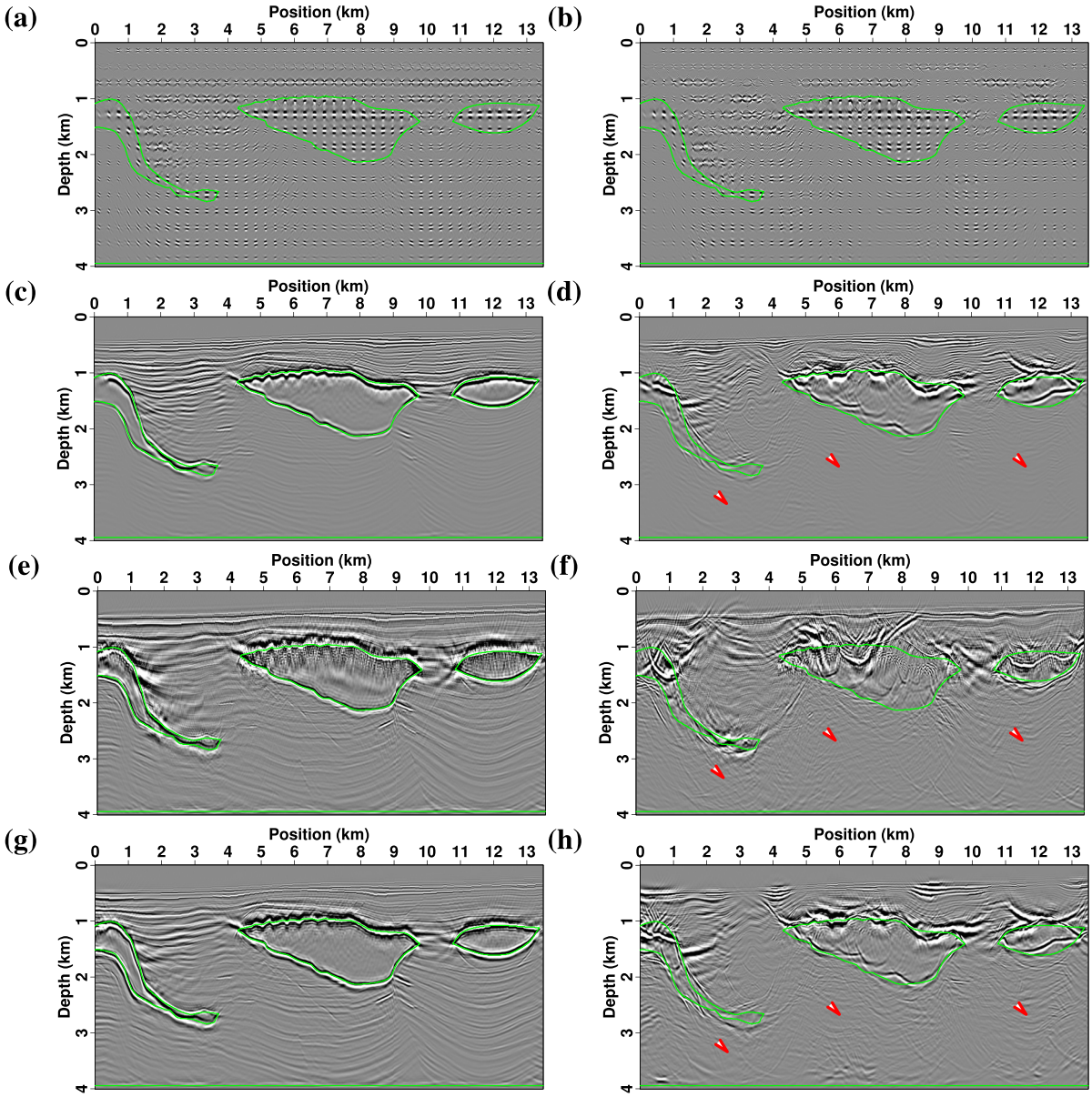

Figure 16. Point-spread functions (PSFs) and migration results using inaccurate velocities with 2% (left column) and 10% (right column) errors. (a, b) PSFs, (c, d) adjoint migration results, (e, f) data-domain least-squares migration (LSM) results, and (g, h) the proposed PSF deconvolution results. The green solid lines denote the boundaries of the salt bodies.

with depths <2 km (Figures 19b, 20c, and 20d). Detailed analysis for data residuals and misfit gradients reveals that the data-domain LSM is trapped in a local minimum because of inaccurate migration velocity model, which leads to many artifacts during data fitting. The proposed method does involve the data fitting and reduces the Hessian blurring effect using image-domain deconvolution. This enables us to obtain a high-resolution image, while not introducing data swing noise (Figures 19c, 20e, and 20f). Comparisons of depth logs in Figure 21 demonstrate that the PSF deconvolution can enhance image amplitudes for deep layers compared to the adjoint migration, and produces similar amplitudes as those in the data-domain LSM.

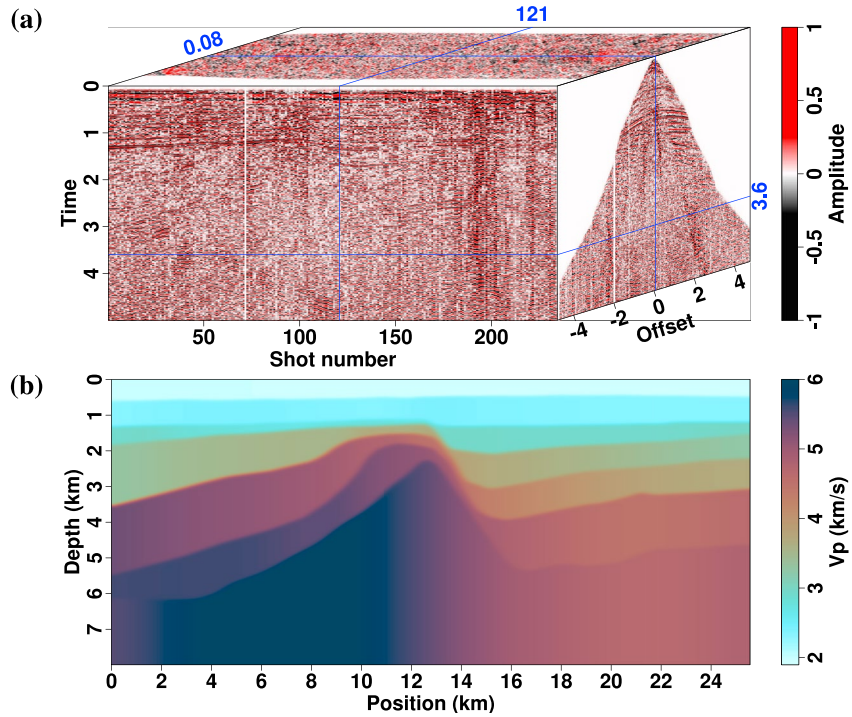

Figure 17. Common-source data (a) and migration velocity model (b) for a land survey.

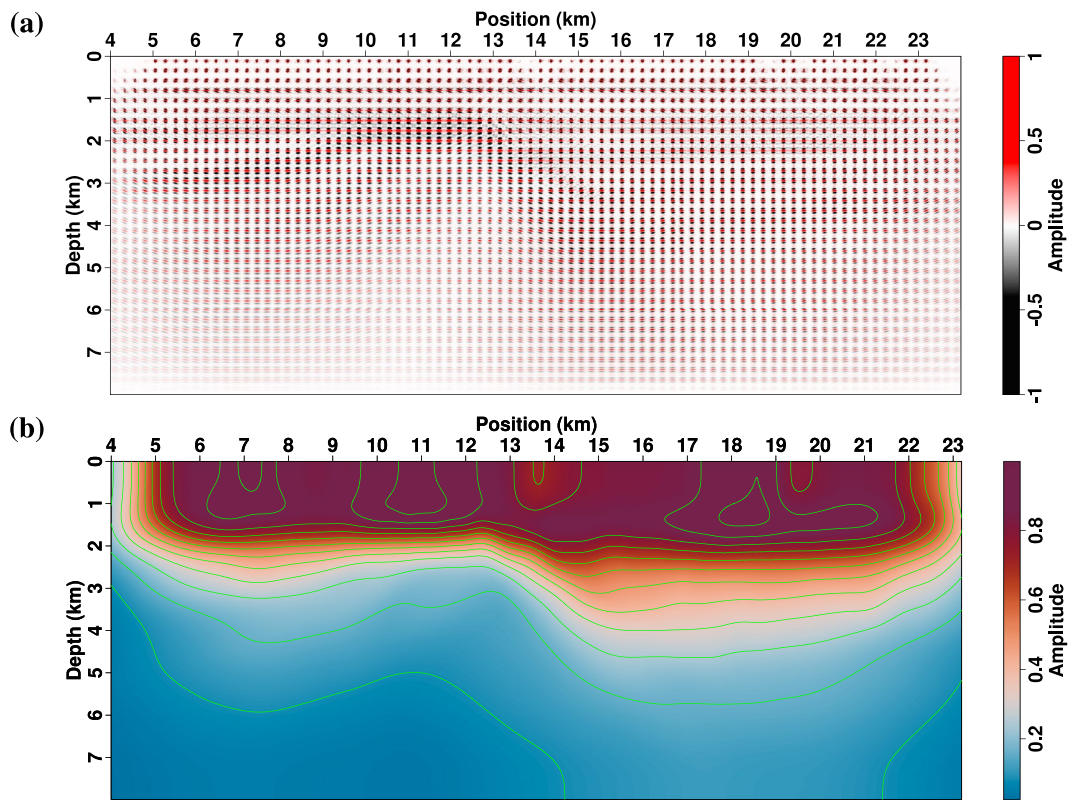

Figure 18. The point-spread functions (PSFs) (a) for the land survey computed using the proposed method and the extracted diagonal Hessian (b). The green lines in panel (b) are the contours of the diagonal Hessian.

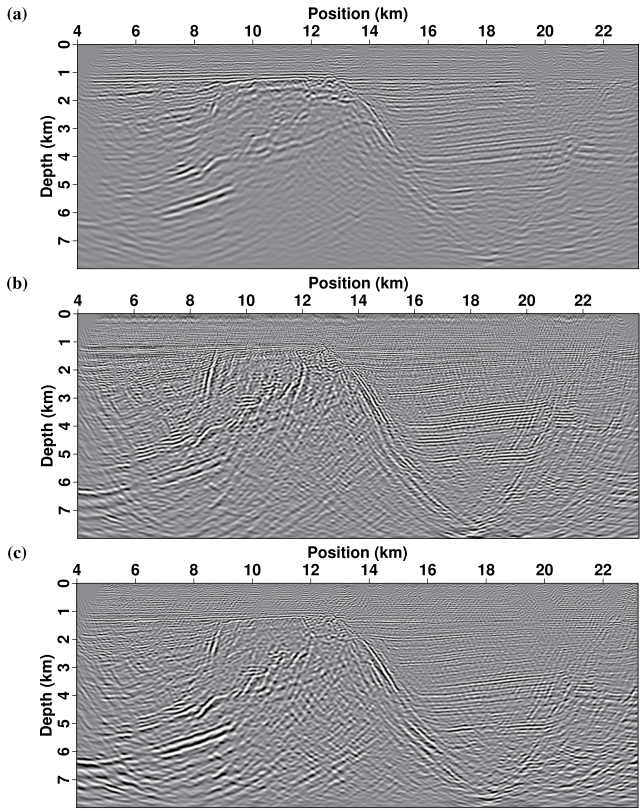

Figure 19. Migration results for the land survey using different methods. (a) Traditional adjoint migration, (b) data-domain least-squares migration (LSM) after eight iterations, and (c) the proposed point-spread function (PSF) deconvolution.

4. Discussion

In this study, we present an efficient PSF calculation method and utilize the PSF deconvolution to improve the seismic imaging quality. Numerical examples for two benchmark models and a land survey verify the feasibility and adaptability of the proposed method for imaging steeply dipping faults, complicated salt structures, and field data with low signal-to-noise ratio. The PSF calculation only depends on acquisition geometry, migration velocity models, and source signature, and does not involve the data fitting procedure. Although the migration velocity may differ from the true velocity model, the PSFs can always be focused while the locations may be inaccurate. In contrast, data-domain LSM estimates subsurface reflectivity by fitting observed data with synthetic seismograms. With inaccurate migration velocity, near-offset data may be fitted well, but far-offset events may not, which will introduce strong artifacts in the reflectivity image. Therefore, the PSF deconvolution is less sensitive to velocity errors in comparison to conventional data-domain LSM.

The key step in the calculation is the modeling and migration. We store the modeling data generated by the scatterers only in a short time window, and migrate these local waveforms in a limited subsurface-offset domain. The local features in modeling and migration enable efficient computation of the PSFs and achieve high-quality images. Numerical experiments (Table 1) show that the proposed method uses less than half of the computational times of conventional data-domain LSM. In addition, the grid spacing and window sizes of the PSFs are independent in the proposed method. This allows in principle to resolve one of the main issues of the wave-equation image-domain PSF method. A large window may be needed to include the whole PSF, and a small spacing may be desirable to follow accurately the spatial variation of the PSFs, particularly in complex heterogeneous media. Hence, high-performance computing technologies using multicore central processors and graphics processing units can be used to further accelerate the computations of PSFs and deconvolution. These strategies provide a great potential to apply the proposed method for large-scale 3D problems.

We utilize the Gaussian beam summation method to compute the Green's function in this study, in which the beam tracing results are stored in the memory and repeatably used. The local modeling and migration as well as PSF deconvolution enable us to avoid the overlapping issue in PSF calculation, while requiring a relatively small computational cost. The similar strategies can also be extended to the wave equation imaging methods. But in the wave equation migrations, especially for reverse-time migration scheme, calculating and storing synthetic data for subsurface scatterers independently requires solving many times of the wave equation. The computational cost will be significantly increased compared with the beam propagator. How to improves the efficiency of PSF deconvolution for wave equation imaging methods needs systematic investigations in the future. In addition, the PSF deconvolution can also be extended to angle-domain migration to produce amplitude-preserved common-image gathers, which are important in amplitude-versus-angle analysis for fluid detection. In the numerical examples, we set the window size as $2\lambda_{max}$. To test the influence of window sizes, we also compute the PSF deconvolution results using 4λ and λ for the field data. The resulting images (Figure 22) do not show large differences, indicating the proposed method is not very sensitive to the selection of window sizes.

We apply the PSF deconvolution only to seismic imaging in acoustic media. It can also be extended to elastic media, for which four PSFs are needed to compute at each location, i.e., P-P, P-S, S-P, and S-S components (Feng et al., 2018). Applying elastic PSFs to PP and PS images not only helps to improve spatial resolution and compensates for irregular illumination, but also corrects crosstalk artifacts between *P* and *S* wave modes. Incorporating seismic attenuation and anisotropy into the PSF calculation is also important in some specific geological environments, such as gas reservoir and fractured shales. It can produce more accurate seismic imaging results in terms of both kinematic and dynamic information.

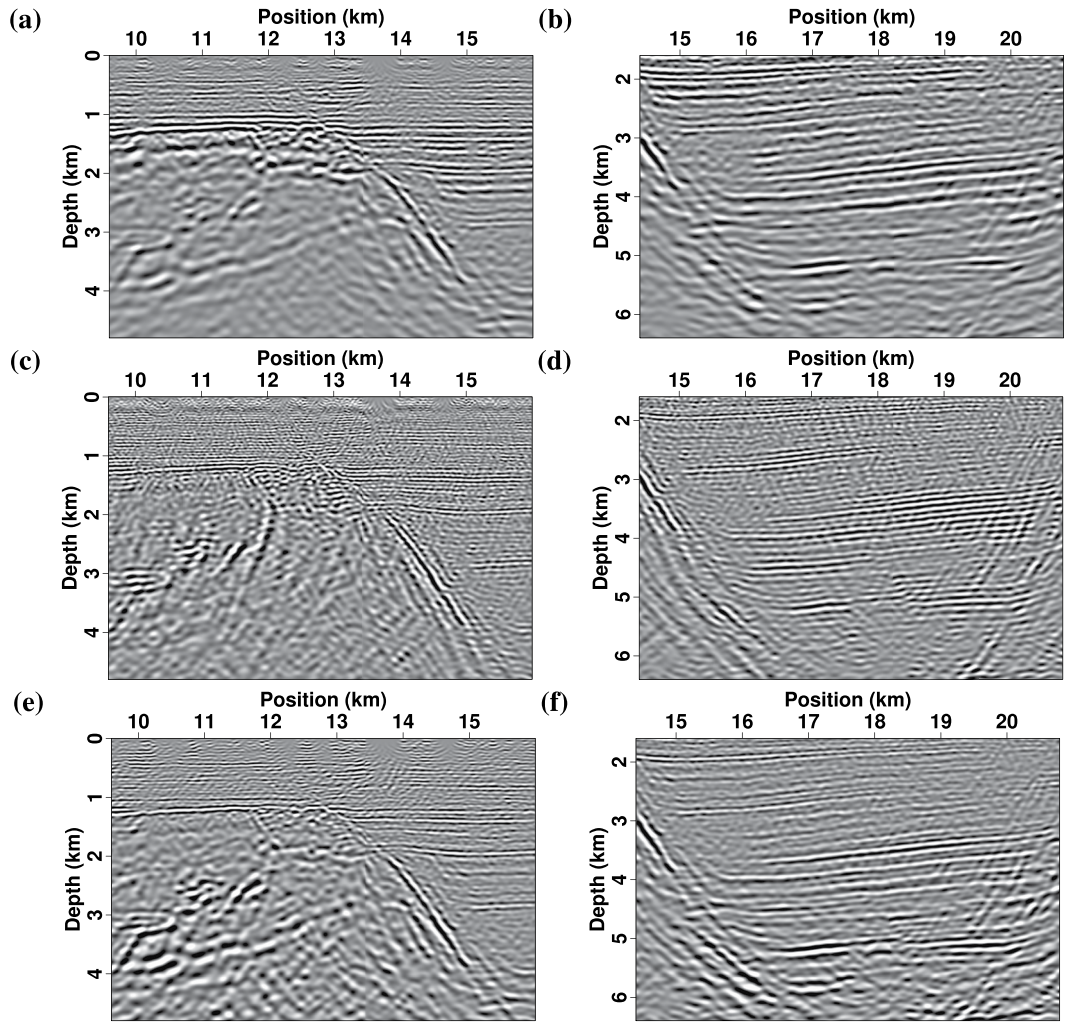

Figure 20. Enlarged migration results for the land survey in two regions. Left column is for the region in $x = [9.6, 16\ \text{km}]$ and $z = [0, 4.8\ \text{km}]$, and right column is for the region in $x = [14.4, 20.8\ \text{km}]$ and $z = [1.6, 6.4\ \text{km}]$. (a, b) Traditional adjoint migration results, (c, d) data-domain least-squares migration (LSM) results, and (e, f) the proposed point-spread function (PSF) deconvolution results.

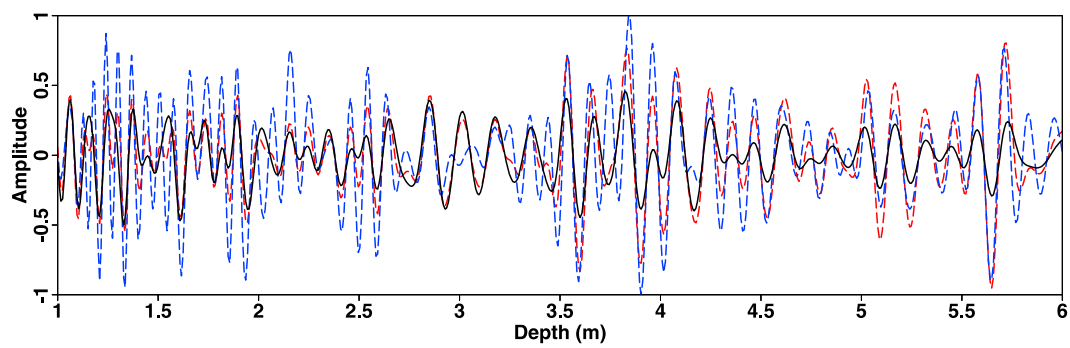

Figure 21. Comparison of depth logs at $x = 17.6$ km. Black solid line denotes the traditional adjoint migration result, blue dashed line denotes the data-domain least-squares migration (LSM) result, and red dashed line denotes the point-spread function (PSF) deconvolution result. Note that the oscillations of the blue dashed line from 1 to 2 km are the faked events in data-domain LSM.

Table 1
Comparisons of Computation Cost Between Data-Domain Least-Squares Migration (LSM) and Point-Spread Function (PSF) Deconvolution for the Three Numerical Examples

Models	Data-domain LSM (hr)	PSF deconvolution (hr)
Marmousi	14.72	6.82
Pluto salt	16.08	7.69
Field data	17.35	8.05

Note. All examples are tested on a workstation with Intel(R) Xeon(R) Gold 5220R CPU @ 2.20 GHz.

5. Conclusions

To avoid the large cost of conventional data-domain LSM, we present an efficient and stable PSF deconvolution method using a Gaussian Beam propagator. The grid spacing and window size of the PSFs are independent, which alleviates the limitation of wave-equation image-domain PSF method on the choice of these two parameters. The PSFs on a coarse grid are first computed using local modeling and migration, and are then interpolated onto a fine image grid on the fly. Next, partition of unity is used to decompose the adjoint migration result into local images that have the same window size as the PSFs. Finally, we deconvolve these local images by the PSFs in the wavenumber domain to compensate for deep amplitudes and alleviate the Hessian blurring effect. Numerical examples for both synthetic and field data demonstrate that the proposed PSF deconvolution can significantly improve image resolution and enhance amplitudes for deep reflectors, while not producing artifacts associated with large-amplitude events as the data-domain LSM. In addition, the PSF deconvolution has the same sensitivity to velocity errors, as traditional adjoint migration, and it is not as sensitive as data-domain LSM.

Appendix A

In a homogeneous medium with P wave velocity v, the Green's function for the outgoing wavefield can be expressed as

$$G(\mathbf{x},\mathbf{x}_0,t)=\frac{\delta\left(t-r(\mathbf{x},\mathbf{x}_0)/v\right)}{4\pi r(\mathbf{x},\mathbf{x}_0)}, \tag{A1}$$

where $\delta(t)$ is the Kronecker delta function and $r(\mathbf{x}, \mathbf{x}_0)$ is the distance from $\mathbf{x}_0$ to $\mathbf{x}$. Inserting Equation A1 into Equation 19, we have

$$\begin{aligned}P_{sf}(\mathbf{x},\mathbf{h})=\sum\nolimits_{\mathbf{x}_s,\mathbf{x}_r}\frac{4}{v^4}\int\left[\frac{\partial^2}{\partial t^2}\frac{f\left(t-r(\mathbf{x}_r,\mathbf{x})/v-r(\mathbf{x},\mathbf{x}_s)/v\right)}{16\pi^2 r(\mathbf{x}_r,\mathbf{x})\,r(\mathbf{x},\mathbf{x}_s)}\right]\\ \times\left[\frac{\partial^2}{\partial t^2}\frac{f\left(t-r(\mathbf{x}_r,\mathbf{x}+\mathbf{h})/v-r(\mathbf{x}+\mathbf{h},\mathbf{x}_s)/v\right)}{16\pi^2 r(\mathbf{x}_r,\mathbf{x}+\mathbf{h})\,r(\mathbf{x}+\mathbf{h},\mathbf{x}_s)}\right]dt,\end{aligned} \tag{A2}$$

By defining

$$\begin{aligned}r(\mathbf{x}_r,\mathbf{x},\mathbf{x}_s)&=r(\mathbf{x}_r,\mathbf{x})+r(\mathbf{x},\mathbf{x}_s),\\ A(\mathbf{x}_r,\mathbf{x},\mathbf{x}_s)&=r(\mathbf{x}_r,\mathbf{x})\,r(\mathbf{x},\mathbf{x}_s),\end{aligned} \tag{A3}$$

Equation A2 can be simplified as

$$P_{sf}(\mathbf{x},\mathbf{h})=\sum_{\mathbf{x}_s,\mathbf{x}_r}\frac{1}{64\pi^4 v^4}\int\left[\frac{\partial_t^2 f\left(t-\left(r(\mathbf{x}_r,\mathbf{x}+\mathbf{h},\mathbf{x}_s)-r(\mathbf{x}_r,\mathbf{x},\mathbf{x}_s)\right)/v\right)\partial_t^2 f(t)}{A(\mathbf{x}_r,\mathbf{x},\mathbf{x}_s)\,A(\mathbf{x}_r,\mathbf{x}+\mathbf{h},\mathbf{x}_s)}\right]dt. \tag{A4}$$

Equation A4 shows that the main energy of PSF focus in a region with the travel time difference less than a period of the source wavelet, and thus we have the following inequality as:

$$\Delta\tau=\frac{r(\mathbf{x}_r,\mathbf{x}+\mathbf{h},\mathbf{x}_s)-r(\mathbf{x}_r,\mathbf{x},\mathbf{x}_s)}{v}<\frac{1}{f_{\min}}, \tag{A5}$$

where $f_{\min}$ is the minimum effective frequency of seismic data. Considering the far field approximation

$$|r(\mathbf{x}_r,\mathbf{x}+\mathbf{h},\mathbf{x}_s)-r(\mathbf{x}_r,\mathbf{x},\mathbf{x}_s)|\approx|\mathbf{e}_h\cdot(\mathbf{e}_s+\mathbf{e}_r)||\mathbf{h}|\le 2|\mathbf{h}|, \tag{A6}$$

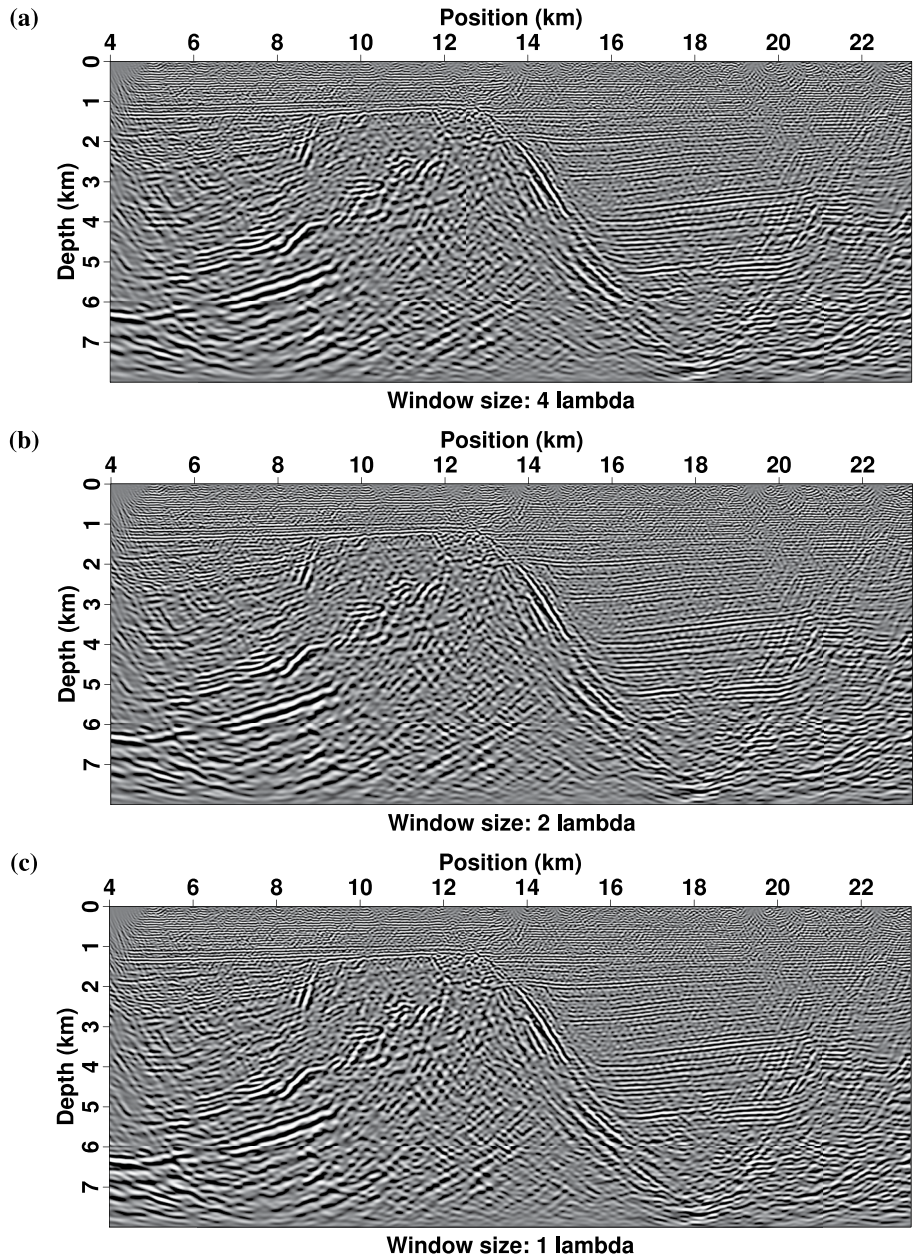

Figure 22. Comparisons of the point-spread function (PSF) deconvolution results of the field data using the window size as (a) $4\lambda_{max}$, (b) $2\lambda_{max}$, and (c) λ_{max}.

Equation A5 can be simplified as

$$|\mathbf{e}_h \cdot (\mathbf{e}_s + \mathbf{e}_r)\,||\mathbf{h}| = \Delta\tau v < \frac{v}{f_{\min}} = \lambda_{\max}, \tag{A7}$$

where $\mathbf{e}_s$, $\mathbf{e}_r$, and $\mathbf{e}_h$ are the unit vectors of source ray, receiver ray, and subsurface offset, respectively, and λ_{max} is the maximum wavelength. Equations A5 and A7 demonstrate that the displacement normal to the effective illumination vector $\mathbf{e}_i = \frac{1}{2}(\mathbf{e}_s + \mathbf{e}_r)$ for a pair of source-receiver ray path can be large (Figure A1a). But with increasing angle illumination from different sources and receivers, the PSFs become focused in a small region (Figures A1b and A1c). This is because many stackings over different incident angles results in $\sum_{\mathbf{e}_i}(\mathbf{e}_h \cdot \mathbf{e}_i)$ approximating a constant. In heterogeneous media, the wavelength depends on subsurface velocities and is spatially varying. To

avoid damaging the effective energy of PSFs, we choose the half width of PSF window as $2\lambda_{\max}$ and thus the subsurface offset satisfies

$$|\mathbf{h}| < 2\lambda_{\max}, \tag{A8}$$

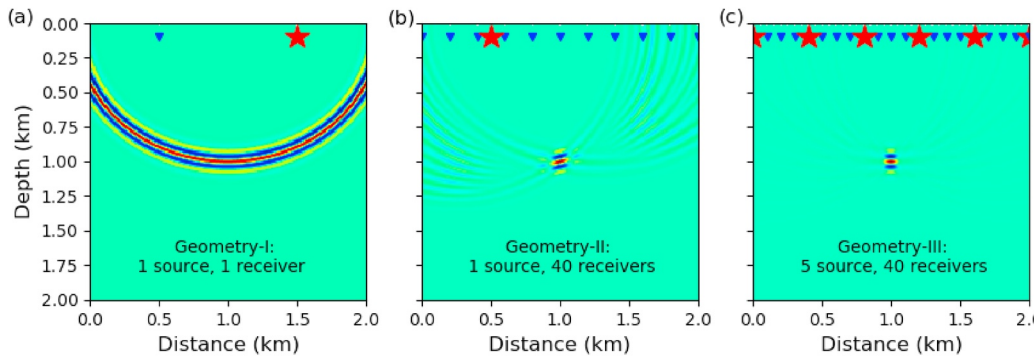

Figure A1. The typical point-spread functions (PSFs) in a homogeneous medium with three different source-receiver configurations.

In addition, it should be noted that when the range of incident angle is limited due to strong lateral velocity variations, e.g., subsalt or beneath/near regions of strong heterogeneous attenuation, the PSFs will be sprayed in a large subsurface region and the truncated PSFs using local Gaussian windows may limit the ability to restore some wavenumbers and introduce artifacts.

Appendix B

In the frequency domain, the Green's functions can be calculated using the Gaussian beam summation as

$$G(\mathbf{x};\mathbf{x}_0,\omega) = \frac{i\omega}{2\pi}\iint \frac{dp_x dp_z}{p_z}\sqrt{\frac{v_0(\mathbf{x})\det\mathbf{Q}(\mathbf{x}_0)}{v_0(\mathbf{x}_0)\det\mathbf{Q}(\mathbf{x})}}\exp\left[i\omega\left(\tau(\mathbf{x})+\frac{1}{2}\mathbf{q}^T(\mathbf{x})\mathbf{P}(\mathbf{x})\mathbf{Q}^{-1}(\mathbf{x})\mathbf{q}(\mathbf{x})\right)\right], \tag{B1}$$

where $\mathbf{x}_0$ is the starting location, ω is the angular frequency, p_x, p_y, and p_z are the components of the ray parameter, $\mathbf{P}$ and $\mathbf{Q}$ are 2×2 complex-valued matrices and can be computed using dynamic ray tracing (Červený et al., 1982; Popov, 2002), det denotes the determinant of a matrix, τ is the travel time along a central ray, and $\mathbf{q}$ denotes a 2D orthogonal coordinate perpendicular to the central rays and it constructs a ray-centered coordinate system combined with the arc length. By denoting

$$\begin{aligned} A(\mathbf{x};\mathbf{x}_0) &= \sqrt{\frac{v_0(\mathbf{x})\det\mathbf{Q}(\mathbf{x}_0)}{v_0(\mathbf{x}_0)\det\mathbf{Q}(\mathbf{x})}}, \\ T(\mathbf{x};\mathbf{x}_0) &= \tau(\mathbf{x})+\frac{1}{2}\mathbf{q}^T(\mathbf{x})\mathbf{P}(\mathbf{x})\mathbf{Q}^{-1}(\mathbf{x})\mathbf{q}(\mathbf{x}), \end{aligned} \tag{B2}$$

and applying the reciprocity for receiver-side wavefield, the complex-valued two-way amplitude and travel time starting from source location $\mathbf{x}_s$, through subsurface scatterer $\mathbf{x}$, and arriving at receiver location $\mathbf{x}_r$ can be expressed as

$$\begin{aligned} A(\mathbf{x}_r;\mathbf{x};\mathbf{x}_s) &= A(\mathbf{x};\mathbf{x}_s)\,A(\mathbf{x};\mathbf{x}_r), \\ T(\mathbf{x}_r;\mathbf{x};\mathbf{x}_s) &= T(\mathbf{x};\mathbf{x}_s)+T(\mathbf{x};\mathbf{x}_r), \end{aligned} \tag{B3}$$

where subscripts s and r denote the source-side and receiver-side variables. Inserting Equations B1–B3 into Equation 19 and applying the inverse Fourier transform yield the PSFs as in Equation 21.

Data Availability Statement

The data sets used in this paper can be download from Harvard Dataverse (https://doi.org/10.7910/DVN/GT0TBT).

Acknowledgments
We appreciate the comments and suggestions from editor M. Bostock, reviewer P. Williamson, and another anonymous reviewer, which significantly improve the manuscript. We are thankful for the support from the funds of the National Key R&D Program of China (2019YFC0605503), the Major Scientific and Technological Projects of CNPC (ZD2019-183-003), the Major projects during the 14th Five-year Plan period under contract number 2021QNLM020001, the National Outstanding Youth Science Foundation (41922028), and Creative Research Groups of China (41821002). J. Y. was supported by the startup funding (20CX06069A) of Guanghua Scholar at the Geophysics Department, China University of Petroleum (East China). G. M. was supported by the Sponsors of UT-Dallas Geophysical Consortium with the contribution number of 1690.

References

Červený, V., Popov, M. M., & Pšenčík, I. (1982). Computation of wave fields in inhomogeneous media-Gaussian beam approach. *Geophysical Journal International*, *70*, 109–128.
Aki, K., & Richards, P. (1980). *Quantitative seismology: Theory and methods*. San Francisco: WH Freeman and Company.
Allwright, C. (1976). Conjugate gradient versus steepest descent. *Journal of Optimization Theory and Applications*, *20*(1), 129–134. https://doi.org/10.1007/bf00933351
Aoki, N., & Schuster, G. T. (2009). Fast least-squares migration with a deblurring filter. *Geophysics*, *74*(6), WCA83–WCA93. https://doi.org/10.1190/1.3155162
Bale, R., Grossman, J., Margrave, G., & Lamoureux, M. (2002). Multidimensional partitions of unity and Gaussian terrains. *CREWES Research Report*, *14*. Retrieved from https://www.researchgate.net/publication/265182366
Baysal, E., Kosloff, D. D., & Sherwood, J. W. (1983). Reverse time migration. *Geophysics*, *48*(11), 1514–1524. https://doi.org/10.1190/1.1441434
Bourgeois, A., Bourget, M., Lailly, P., Poulet, M., Ricarte, P., & Versteeg, R. (1990). *Marmousi, model and data*. In EAEG workshop (Vol. 108).
Claerbout, J. F. (1985). *Imaging the earth's interior* (Vol. 1). Oxford: Blackwell Scientific Publications.
Dai, W., Fowler, P., & Schuster, G. (2012). Multi-source least-squares reverse time migration. *Geophysical Prospecting*, *60*(4), 681–695. https://doi.org/10.1111/j.1365-2478.2012.01092.x
Dai, W., Wang, X., & Schuster, G. (2011). Least-squares migration of multisource data with a deblurring filter. *Geophysics*, *76*(5), R135–R146. https://doi.org/10.1190/geo2010-0159.1
Dutta, G., & Schuster, G. T. (2014). Attenuation compensation for least-squares reverse time migration using the viscoacoustic-wave equation. *Geophysics*, *79*(6), S251–S262. https://doi.org/10.1190/geo2013-0414.1
Feng, Z., Guo, B., & Schuster, G. T. (2018). Multiparameter deblurring filter and its application to elastic migration and inversion. *Geophysics*, *83*(5), S421–S435. https://doi.org/10.1190/geo2017-0572.1
Feng, Z., & Schuster, G. T. (2017). Elastic least-squares reverse time migration. *Geophysics*, *82*(2), S143–S157. https://doi.org/10.1190/geo2016-0254.1
Fletcher, R., Nichols, D., Bloor, R., & Coates, R. (2016). Least-squares migration—Data domain versus image domain using point spread functions. *The Leading Edge*, *35*(2), 157–162. https://doi.org/10.1190/tle35020157.1
Fomel, S., Berryman, J. G., Clapp, R. G., & Prucha, M. (2008). Iterative resolution estimation in least-squares Kirchhoff migration. *Geophysical Prospecting*, *50*(6), 577–588.
Freeman, B., Klemperer, L., & Hobbs, W. (1988). The deep structure of northern England and the Iapetus Suture zone from BIRPS deep seismic reflection profiles. *Journal of the Geological Society*, *145*(5), 727–740. https://doi.org/10.1144/gsjgs.145.5.0727
Gazdag, J. (1978). Wave equation migration with the phase-shift method. *Geophysics*, *43*(7), 1342–1351. https://doi.org/10.1190/1.1440899
Gray, S. H. (2001). Seismic imaging. *Geophysics*, *66*(1), 15–17. https://doi.org/10.1190/1.1444892
Gray, S. H., & May, W. P. (1994). Kirchhoff migration using Eikonal equation traveltimes. *Geophysics*, *59*(5), 810–817. https://doi.org/10.1190/1.1443639
Guitton, A. (2004). Amplitude and kinematic corrections of migrated images for nonunitary imaging operators. *Geophysics*, *69*(4), 1017–1024. https://doi.org/10.1190/1.1778244
Guitton, A. (2017). Preconditioned 3D least-squares RTM with non-stationary matching filters. *Paper presented at the 79th EAGE Conference and Exhibition* (Tu A1-06). https://doi.org/10.3997/2214-4609.201700802
Guo, S., & Wang, H. (2019). Image domain least-squares migration with a Hessian matrix estimated by non-stationary matching filters. *Journal of Geophysics and Engineering*, *17*(1), 148–159. https://doi.org/10.1093/jge/gxz098
Hill, R. (1990). Gaussian beam migration. *Geophysics*, *55*(11), 1416–1428. https://doi.org/10.1190/1.1442788
Hill, R. (2001). Prestack Gaussian-beam depth migration. *Geophysics*, *66*(4), 1240–1250. https://doi.org/10.1190/1.1487071
Hokstad, K. (2000). Multicomponent Kirchhoff migration. *Geophysics*, *65*(3), 861–873. https://doi.org/10.1190/1.1444783
Hou, J., & Symes, W. W. (2015). An approximate inverse to the extended born modeling operator. *Geophysics*, *80*(6), R331–R349. https://doi.org/10.1190/geo2014-0592.1
Keho, T. H., & Beydoun, W. B. (1988). Paraxial ray Kirchhoff migration. *Geophysics*, *53*(12), 1540–1546. https://doi.org/10.1190/1.1442435
Latter, T., Gregory, M., Ratcliffe, A., Roberts, G., Xiao, B., Sood, R., & Purcell, C. (2018). *Imaging through near-surface absorption bodies with viscoacoustic least-squares migration: A case study from the Northern Viking Graben* (pp. 4316–4320). SEG Technical Program Expanded Abstracts.
Lu, S., Liu, F., Chemingui, N., Valenciano, A., & Long, A. (2018). Least-squares full-wavefield migration. *The Leading Edge*, *37*(1), 46–51. https://doi.org/10.1190/tle37010046.1
McMechan, G. A. (1983). Migration by extrapolation of time-dependent boundary values. *Geophysical Prospecting*, *31*(3), 413–420. https://doi.org/10.1111/j.1365-2478.1983.tb01060.x
Meza, C. (2010). Steepest descent. *WIREs Computational Statistics*, *2*(6), 719–722. https://doi.org/10.1002/wics.117
Nemeth, T., Wu, C., & Schuster, G. T. (1999). Least-squares migration of incomplete reflection data. *Geophysics*, *64*(1), 208–221. https://doi.org/10.1190/1.1444517
Nguyen, B. D., & McMechan, G. A. (2015). Five ways to avoid storing source wavefield snapshots in 2D elastic prestack reverse time migration. *Geophysics*, *80*(1), S1–S18. https://doi.org/10.1190/geo2014-0014.1
Plessix, R.-E., & Mulder, W. A. (2004). Frequency-domain finite-difference amplitude-preserving migration. *Geophysical Journal International*, *157*(3), 975–987. https://doi.org/10.1111/j.1365-246x.2004.02282.x
Popov, M. (2002). *Ray theory and Gaussian beam method for geophysicists*. Editora da Universidade Federal da Bahia.
Pratt, R. G., Shin, C., & Hick, G. J. (1998). Gauss-Newton and full Newton methods in frequency-space seismic waveform inversion. *Geophysical Journal International*, *133*(2), 341–362. https://doi.org/10.1046/j.1365-246X.1998.00498.x
Ren, Z., Liu, Y., & Sen, M. K. (2017). Least-squares reverse time migration in elastic media. *Geophysical Journal International*, *208*(2), 1103–1125. https://doi.org/10.1093/gji/ggw443

Rickett, J. E. (2003). Illumination-based normalization for wave-equation depth migration. *Geophysics*, *68*(4), 1371–1379. https://doi.org/10.1190/1.1598130

Scales, J. A. (1987). Tomographic inversion via the conjugate gradient method. *Geophysics*, *52*(2), 179–185. https://doi.org/10.1190/1.1442293

Shin, C., Jang, S., & Min, D. (2001). Improved amplitude preservation for prestack depth migration by inverse scattering theory. *Geophysical Prospecting*, *49*(5), 592–606. https://doi.org/10.1046/j.1365-2478.2001.00279.x

Stoffa, P., Fokkema, J. T., de Luna Freire, R., & Kessinger, W. (1990). Split-step Fourier migration. *Geophysics*, *55*(4), 410–421. https://doi.org/10.1190/1.1442850

Stoughton, D., Stefani, J., & Michell, S. (2001). *2D elastic model for wavefield investigations of subsalt objectives, deep water Gulf of Mexico* (pp. 1269–1272). SEG Technical Program Expanded Abstracts.

Sun, R., & McMechan, G. A. (2001). Scalar reverse-time depth migration of prestack elastic seismic data. *Geophysics*, *66*(5), 1519–1527. https://doi.org/10.1190/1.1487098

Tang, Y. (2009). Target-oriented wave-equation least-squares migration/inversion with phase-encoded Hessian. *Geophysics*, *74*(6), WCA95–WCA107. https://doi.org/10.1190/1.3204768

Tarantola, A. (1984a). Inversion of seismic reflection data in the acoustic approximation. *Geophysics*, *49*(8), 1259–1266. https://doi.org/10.1190/1.1441754

Tarantola, A. (1984b). Linearized inversion of seismic reflection data. *Geophysical Prospecting*, *32*(6), 998–1015. https://doi.org/10.1111/j.1365-2478.1984.tb00751.x

Valenciano, A. A., Biondi, B., & Guitton, A. (2006). Target-oriented wave-equation inversion. *Geophysics*, *71*(4), A35–A38. https://doi.org/10.1190/1.2213359

Virieux, J., & Operto, S. (2009). An overview of full-waveform inversion in exploration geophysics. *Geophysics*, *74*(6), WCC1–WCC26. https://doi.org/10.1190/1.3238367

Wang, X., Dai, W., & Schuster, G. T. (2013). *Regularized plane-wave least-squares Kirchhoff migration* (pp. 3242–3246). SEG Technical Program Expanded Abstracts.

Wiggins, J. W. (1984). Kirchhoff integral extrapolation and migration of nonplanar data. *Geophysics*, *49*(8), 1239–1248. https://doi.org/10.1190/1.1441752

Wong, M., Biondi, B. L., & Ronen, S. (2015). Imaging with primaries and free-surface multiples by joint least-squares reverse time migration. *Geophysics*, *80*(6), S223–S235. https://doi.org/10.1190/geo2015-0093.1

Wong, M., Ronen, S., & Biondi, B. (2011). *Least-squares reverse time migration/inversion for ocean bottom data: A case study* (pp. 2369–2373). SEG Technical Program Expanded Abstracts.

Xue, Z., Chen, Y., Fomel, S., & Sun, J. (2016). Seismic imaging of incomplete data and simultaneous-source data using least-squares reverse time migration with shaping regularization. *Geophysics*, *81*(1), S11–S20. https://doi.org/10.1190/geo2014-0524.1

Yan, J., & Sava, P. (2008). Isotropic angle-domain elastic reverse-time migration. *Geophysics*, *73*(6), S229–S239. https://doi.org/10.1190/1.2981241

Yang, J., Hua, B., Williamson, P., Zhu, H., McMechan, G., & Huang, J. (2020). Elastic least-squares imaging in tilted transversely isotropic media for multicomponent land and pressure marine data. *Surveys in Geophysics*, *41*, 805–833. https://doi.org/10.1007/s10712-020-09588-3

Yang, J., Huang, J., Li, Z., Zhu, H., McMechan, G. A., & Luo, X. (2021). Approximating the Gauss-Newton Hessian using a space-wavenumber filter and its applications in least-squares seismic imaging. *IEEE Transactions on Geoscience and Remote Sensing*, *1*, 1–13. https://doi.org/10.1109/TGRS.2021.3064852

Yang, J., Zhu, H., McMechan, G., & Yue, Y. (2018). Time-domain least-squares migration using the Gaussian beam summation method. *Geophysical Journal International*, *214*(1), 548–572. https://doi.org/10.1093/gji/ggy142

Yang, K., & Zhang, J. (2019). Comparison between Born and Kirchhoff operators for least-squares reverse time migration and the constraint of the propagation of the background wavefield. *Geophysics*, *84*(5), R725–R739. https://doi.org/10.1190/geo2018-0438.1

Zhang, D., & Schuster, G. T. (2014). Least-squares reverse time migration of multiples. *Geophysics*, *79*(1), S11–S21. https://doi.org/10.1190/geo2013-0156.1

Zhang, Y., Duan, L., & Xie, Y. (2015). A stable and practical implementation of least-squares reverse time migration. *Geophysics*, *80*(1), V23–V31. https://doi.org/10.1190/geo2013-0461.1

Zhang, Y., Zhang, G., & Bleistein, N. (2005). Theory of true-amplitude one-way wave equations and true-amplitude common-shot migration. *Geophysics*, *70*(4), E1–E10. https://doi.org/10.1190/1.1988182